# Rapid slip along the central Altyn Tagh Fault: Morphochronologic evidence from Cherchen He and Sulamu Tagh

A.-S. Mériaux,[1,2] F. J. Ryerson,[2] P. Tapponnier,[1] J. Van der Woerd,[2,3] R. C. Finkel,[2] Xiwei Xu,[4] Zhiqin Xu,[5] and M. W. Caffee[2,6]

Received 28 April 2003; revised 27 January 2004; accepted 23 March 2004; published 8 June 2004.

[1] To better constrain the ongoing rates of deformation in northern Tibet, the ages of fluvial and glacial geomorphic markers left-laterally displaced by the Altyn Tagh Fault have been determined by radiocarbon and $^{10}$Be-$^{26}$Al cosmic ray exposure dating. Two sites were investigated: Cherchen He and Sulamu Tagh, both near Tura (~37.6°N, 86.6°E). The sites are geomorphologically distinct with Cherchen He dominated by fluvial processes and the Sulamu Tagh by glacial action. Nine offsets ranging from 166 to 3660 m with ages between 6 and 113 ka yield an average slip rate of 26.9 ± 6.9 mm/yr. Landscape evolution appears to have been modulated by climate change and is temporally consistent with the $\delta^{18}$O record from the Guliya ice cap in the West Kunlun; the features of interest were all formed by glacial and fluvial processes subsequent to marine isotope stage 5e, with the youngest features having formed during the early Holocene Optimum. This "near-field," morphochronological slip rate is averaged over many earthquake cycles and is hence little affected by interseismic strain. It is kinematically consistent with other, somewhat lower, geomorphic slip rate measurements to the east. The average rate, and lower bounds obtained from alternate interpretational models, 18.4 mm/yr, cannot be reconciled with the most rece geodetic measurements (~7 mm/yr), suggesting that interseismic strain and interactions with adjacent faults may lead to disparate geologic and geodetic rate estimates. This late Pleistocene-Holocene, morphochronologic rate would imply that, at this longitude, the Altyn Tagh Fault, on the north edge of Tibet, might absorb almost as much of India's convergence relative to Siberia as the Himalayan Main Frontal Thrust does on the southern edge of the plateau. *INDEX TERMS:* 1035 Geochemistry: Geochronology; 1208 Geodesy and Gravity: Crustal movements—intraplate (8110); 8102 Tectonophysics: Continental contractional orogenic belts; 8107 Tectonophysics: Continental neotectonics; *KEYWORDS:* slip rates, cosmogenic dating, Indo-Asian collision

**Citation:** Mériaux, A.-S., F. J. Ryerson, P. Tapponnier, J. Van der Woerd, R. C. Finkel, X. Xu, Z. Xu, and M. W. Caffee (2004), Rapid slip along the central Altyn Tagh Fault: Morphochronologic evidence from Cherchen He and Sulamu Tagh, *J. Geophys. Res.*, *109*, B06401, doi:10.1029/2003JB002558.

## 1. Introduction

[2] The Tibetan Plateau is surrounded by large strike-slip faults, such as the Altyn Tagh Fault (ATF), whose role in accommodating Indo-Asian convergence is hotly debated [*Avouac and Tapponnier*, 1993; *England and Houseman*, 1986; *England and Molnar*, 1997a, 1997b; *Peltzer and Saucier*, 1996; *Peltzer and Tapponnier*, 1988]. At one extreme, they are viewed as a by-product of distributed deformation in the lower crust and mantle [*England and Molnar*, 1997a, 1997b]. At the other, they are interpreted as localized lithospheric shear-zones, equivalent to intracontinental plate boundaries [*Avouac and Tapponnier*, 1993; *Peltzer and Saucier*, 1996]. The resolution of this issue, which has implications beyond the tectonics of Tibet, requires quantitative information, not only on the deep structure [*Herquel et al.*, 1999; *Wittlinger et al.*, 1998] but also on the slip rates of these faults. Estimates of the Holocene sinistral slip rate of the central Altyn Tagh Fault vary from 2 to 40 mm/yr [*Ge et al.*, 1992; *Peltzer et al.*, 1989] and cannot be explained by the along strike variations in slip rate [*Peltzer et al.*, 1989; *Meyer et al.*, 1998]. Low slip rates (mm/yr) have been taken to suggest widely distributed, homogeneous deformation [*Bendick et al.*,

[1]Institut de Physique du Globe de Paris, CNRS UMR 7578, Paris, France.
[2]Lawrence Livermore National Laboratory, Livermore, California, USA.
[3]Now at Institut de Physique du Globe de Strasbourg, Ecole et Observatoire des Sciences de la Terre, Strasbourg, France.
[4]Seismological Bureau, Beijing, China.
[5]Institute of Geology, Ministry of Land and Resources, Beijing, China.
[6]Now at Physics Department, Purdue University, West Lafayette, Indiana, USA.


0148-0227/04/2003JB002558$09.00

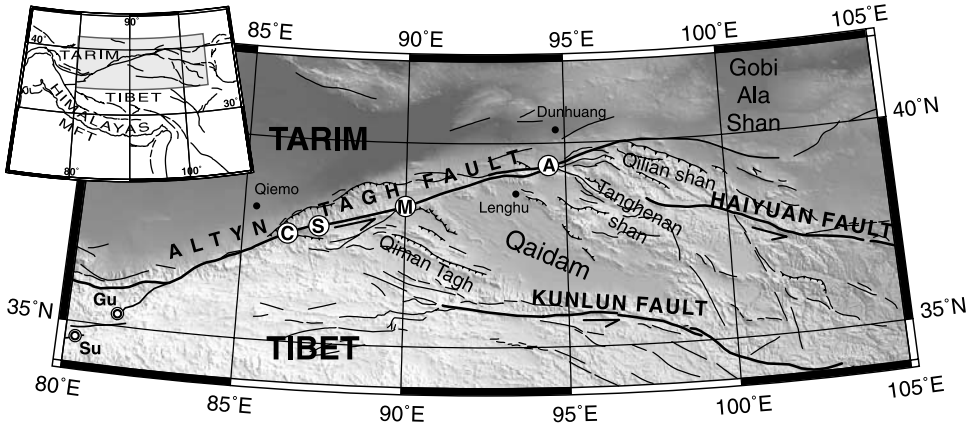


**Figure 1.** Large-scale tectonic map of northern Tibet with this and related studies: C, Cherchen He; S, Sulamu Tagh; M, Mangnai Zhen [*Bendick et al.*, 2000]; A, Aksay [*Mériaux et al.*, 1997]. Local paleoclimatic sites are also indicated: Gu, Guliya Ice cap [*Thompson et al.*, 1997], and Su, Sumxi Co lake [*Gasse et al.*, 1991].

2000; *Chen et al.*, 2000; *Shen et al.*, 2001; *Washburn et al.*, 2001], while fast rates (cm/yr) rule it out [*Avouac and Tapponnier*, 1992; *Peltzer and Saucier*, 1996; *Tapponnier et al.*, 2001].

[3] To quantify better the long-term slip rate on the central stretch of the Altyn Tagh Fault, we present new measurements of the late Pleistocene-Holocene slip rate at two sites near Tura: the Cherchen He and Sulamu Tagh (Figure 1). In this region, the fault closely follows the Sulamu Range front, and meter-sized pressure ridges attest to the occurrence of large earthquakes along its trace. At this longitude, little slip has yet been transferred to the thrusts that build the mountains of NE Tibet [*Meyer et al.*, 1998]. Hence it is reasonable to expect a maximum slip rate. The slip rate determinations are obtained by restoration of well-defined offsets of fluvial channels, terrace risers, morainic ridges and glacial valleys whose ages are constrained by $^{14}C$ dating of charcoals [cf. *Sieh and Jahns*, 1984] and/or $^{10}Be$-$^{26}Al$ cosmic ray exposure dating of both surface and/or subsurface quartz samples [*Anderson et al.*, 1996; *Hancock et al.*, 1999; *Van der Woerd et al.*, 1998, 2000]. This methodology provides a time-integrated slip rate that spans numerous earthquake cycles, and avoids the potential ambiguities encountered in associating paleoseismic events in vertical trench sections with horizontal surface offsets.

## 2. Geologic and Geomorphic Setting

### 2.1. Cherchen He Site

[4] At this site, north of the Cherchen River (~37.6°N, 86.6°E, 3000–3100 m above sea level (asl)), the N69°E striking ATF offsets terrace risers and surfaces emplaced by tributary streams of the Cherchen river (WS, ES, Figure 2). The key geomorphic features were mapped in the field using SPOT and Corona images (resolution of 10 m and ~3.5 m, respectively) and 1:100,000-scale topographic maps. The offset measurements are based upon total station profiles and SPOT images. The highest terrace level, T3, ~23 m above the western streambed (WS) is preserved only north of the fault. The intermediate level, T2, ~10 m below T3, covers the broadest area on the east bank of the river (Figures 3 and 4), and the ~30 m cliff incised into it by the river exposes thick, fill conglomerates (Figure 4a). The lowest level, T1, is a thinner strath fanglomerate standing ~5.5 m above the present streambed (Figures 3 and 4a).

[5] Near the western stream (WS), both T1 and T2 are made of pebbles (typically 10 cm in diameter) and cobbles (up to 50 cm) of various lithologies including granitic gneisses and pure quartz, intercalated with gravel layers (Figures 4b and 4c). A silty sand matrix fills the interstices. Each surface has very sparse vegetation and is composed of pebbles with a poorly developed soil of coarse sand and silt (Figures 4a and 4b). With few exceptions there is no accumulation of surface loess. The active riser incised in T1 by the present stream (WS) shows no evidence for the formation of any "pavement" of surface pebbles nor near-surface cryoturbation or bioturbation. Where exposed along the Cherchen river cliff, the base of T2 has an irregular topography, indicative of the infilling of preexisting channels incised into older conglomerates (Figure 4a). In contrast, T1 is a layer of uniform thickness (~2.5 m) with a flat base that cuts the underlying conglomerates (Figure 4a), indicating that T1 is a strath terrace responsible for cutting the T2/T1 riser. The surfaces of both terraces are relatively flat, slope toward the river by ~4°, and show no evidence of regressive rill incision along the Cherchen River cliff (Figure 3). On the eastern side of the site, a smaller, less powerful stream, ES, as shown by the finer, more distal nature of its deposits, has emplaced terrace T1 and cut the T2/T1 riser (Figure 2). In section, these deposits include layers of silt and clay intercalated with small gravel beds (Figure 5). Subsurface charcoal samples were collected in the silts and clays below the uppermost gravel bed of T1 (Figure 5). Here, loess has accumulated on the leeward side of the T2/T1 riser, and the surface is covered by soil and vegetation.

[6] A large, abandoned paleochannel (PC) is incised into T2 south of the fault (Figure 2). Between the fault and the Cherchen River, PC is as wide as the active channel of WS north of the fault. This suggests that the only stream

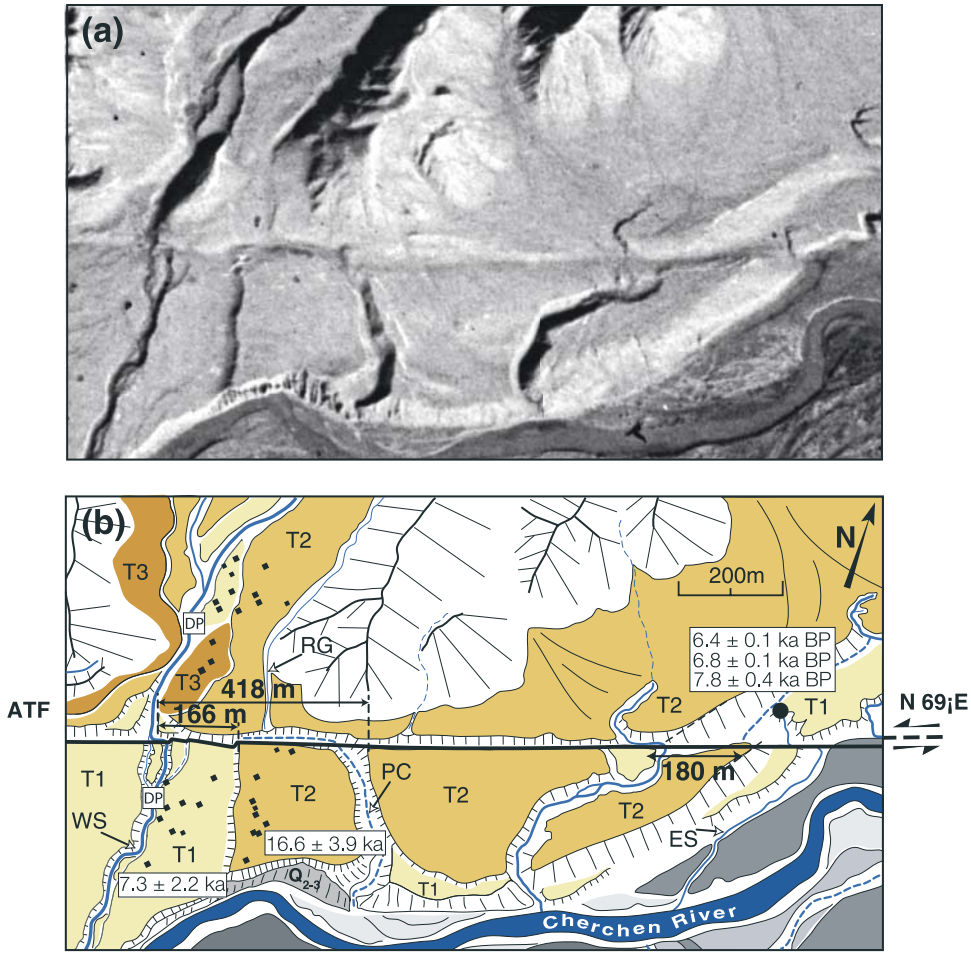


**Figure 2.** Offset terrace risers and channels of tributaries of Cherchen He west of Tura (37.6°N, 86.4°E, ~3000 m asl). (a) Corona image (DS 1025–2118DA031). (b) Results of field mapping. Locations of surface samples are designated as diamonds; DP indicates the locations of subsurface sampling for cosmogenic dating. Terrace surfaces are numbered and shaded as a function of increasing age and elevation. WS is the western stream, ES is the eastern stream, and PC and RG are the paleochannel and regressive channel in incised T2 terrace, respectively. Measured riser and stream offsets and average terrace ages are shown.

powerful enough to incise PC was WS. PC bends to the west along the fault trace and is visible to the T2/T1 riser in spite of postabandonment infilling by colluvium from the fault scarp (Figures 2 and 3). The bend in the channel is likely due its left-lateral displacement, placing its west side in front of the channel position north of the fault and allowing further fluvial erosion. The east bank on the other hand is protected from fluvial erosion by fault motion. A small regressive gully, RG, incises T2 north of the fault. It is bypassed by, and perched above, the westward extension of PC along the fault trace. Moreover, it is too narrow to have fed the PC channel. The channels' relative widths and spatial relationships thus concur and demonstrate that PC represents an ancient course of WS, entrenched into T2.

[7] The T2/T1 fossil riser on the left bank of WS is sinistrally offset by 166 ± 10 m relative to the east edge of the WS channel north of the fault trace. As the eastern edge of the PC channel is protected from fluvial erosion by sinistral fault motion it best preserves the original morphology and position of the channel. Its offset relative to WS's piercing point on the north side of the fault is 418 ± 20 m. The T2/T1 riser cuts the westward extension of PC along the fault, and must therefore postdate the abandonment of PC. This supports the inference that the T2/T1 riser is much younger than the incision of PC, and hence the deposition of T2. The other high, oblique fossil T2/T1 riser along the other tributary stream to the east (ES) is cut and offset 180 ± 10 m by the fault. The uncertainty on the offset measurements is dominated by the width of the feature concerned, its angle to the fault and, where required, projection to the fault.

### 2.2. Sulamu Tagh Site

[8] The Sulamu Tagh site (~37.7°N, 87.4°E, Figure 1) is located 60 km east of the Cherchen He site, at a much greater elevation, between 4400 and 5000 m asl. Here, the N75°E striking ATF cuts a landscape shaped primarily by ice action (Figures 6–9). Emanating from catchments on the highest peaks of the range (>6000 m asl), the two longest glaciers on the south flank of Sulamu Tagh, reach closest to the fault at this site. For at least 20 km east and west of these

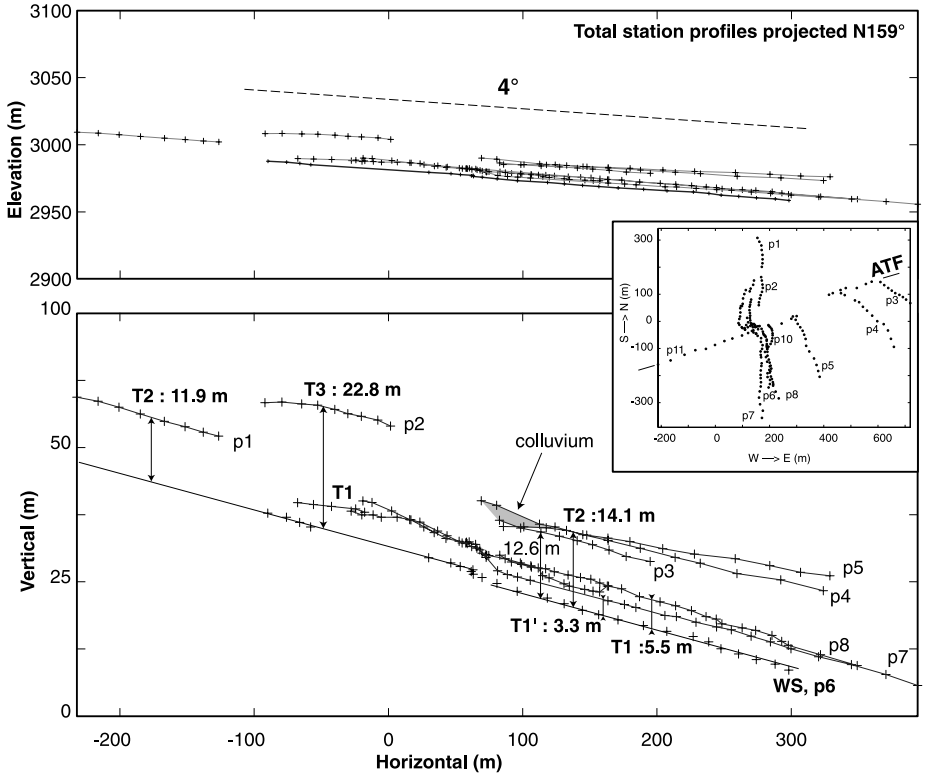


**Figure 3.** Total station profiles projected perpendicular to the average strike of the ATF, N159°. (top) Average slope indicated on the 1 × 1 scale projected profiles; (bottom) projection with vertical exaggeration 4×. Height of terraces above the western stream (WS) is indicated. Inset is a map view of the total station profiles.

active glaciers no comparably large glaciers exist along the fault (Figure 6). Ice ponding at the terminus of the widest, western, glacier (WG, Figures 7 and 8) encroaches across the fault trace, while the more deeply entrenched, eastern glacier (EG) terminates only ~700 m north of it.

[9] Though now essentially free of ice, the area south of the fault bears strong imprint of glacial invasion. Till mantles a flattish, 1–2 km wide, hanging bench, 4600–5000 m high, that stretches along the south side of the fault to about 8 km east of the western glacier terminus (Figures 7 and 8). To the east, the northern edge of this till-mantled surface is defined by a rectilinear, ~100-m-high, north facing wall, incised along the fault by the eastern glacier and its outwash (EO, Figures 8 and 9d). This precipitous north facing wall now isolates the till deposited on the bench from the Sulamu range. South of the wall the till bench slopes gently and narrows to the south, breaching the surrounding relief (Figures 7 and 8). The funnel-like geometry of this passage was carved by the confluence of the western (WG) and eastern (EG) glaciers (Figures 7, 8, and 9a). This paleoglacial confluence, CP, is subdivided by morainic ridges into four broad channels that become deeper from east to west. The principal postglacial streams draining the till bench flow along these channels, between the abandoned lateral moraines (Figures 7 and 8). The highest, best defined moraine, M1, is located along the east side of the deepest, western channel, WC. West of CP, another paleoglacial valley breaches the relief south of the till bench (WV, Figures 7, 8, and 9c), providing an outlet for one of the two main outwashes (CO) of the western glacier. Downstream from its east directed bend, the south side of WV is bounded by another abandoned lateral moraine, M2, with even steeper side slopes and sharper crest than M1 (Figure 9c).

[10] The till and moraines on the bench must have been emplaced by WG and EG when they crossed the fault, during glacial maxima, and before EG deviated eastward along the fault (Figures 7 and 8). Similarly, the western paleoglacial valley can only have been incised by the western glacier before it retreated to pond against relief displaced by the fault. Thus it is clear that both CP and WV have been left-laterally offset large distances from their sources by the ATF.

[11] Reconstruction of the paleoconfluence is achieved by aligning its outer edges with the present eastern and western edges of the eastern, and western glacier valleys, respectively. The displacement estimates are sensitive to relatively small errors (300 m) and yield an offset of 3660 ± 300 m (Figures 10 and 11a). That the separation of the outer edges of glacial incision is the same (~4 km) north and south of the fault further justifies this reconstruction. Retrofitting the deepest channel on the east side of the paleoconfluence, EC (east of M1), with the eastern glacier valley yields an offset of 2080 ± 100 m (Figure 11b). The M1 morainic ridge itself has been displaced 1400 ± 100 m relative to the oblique, ESE trending southeastern edge of the western glacier valley (Figure 11c) The sinistral offset of the eastern edge of the WV paleoglacial valley relative to that of the present

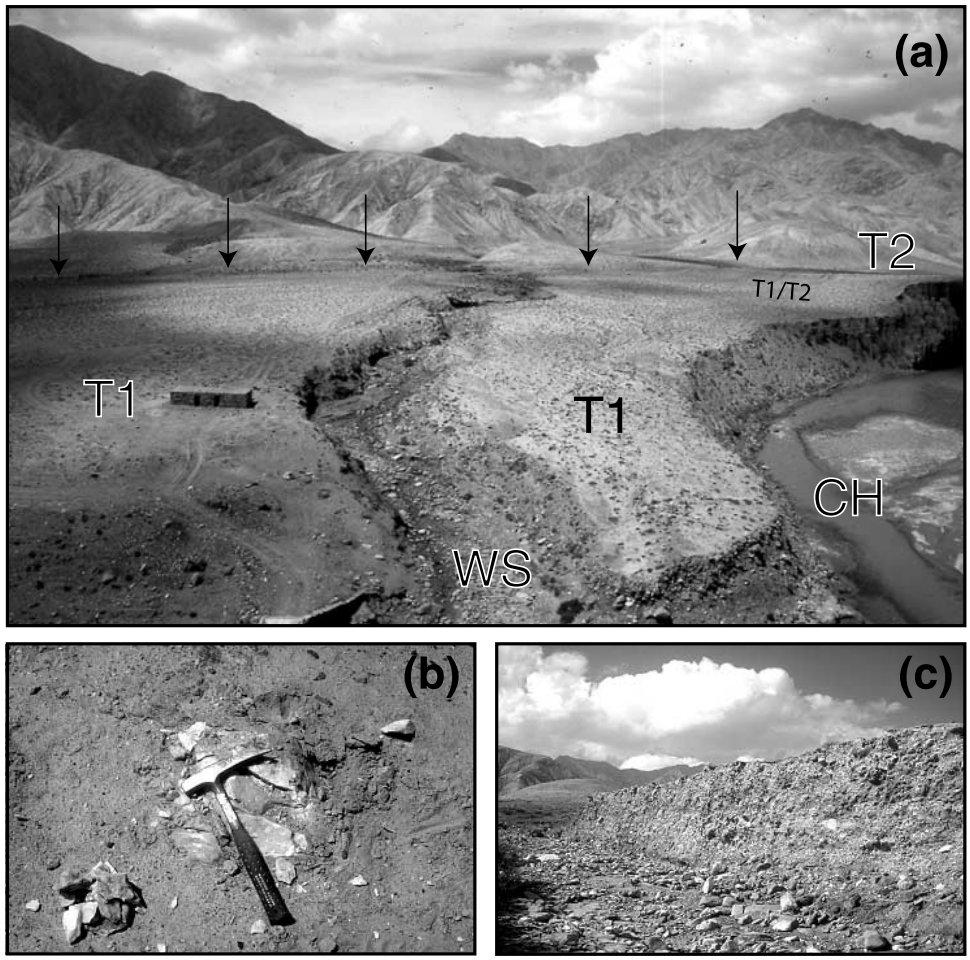


**Figure 4.** Cherchen He site. (a) Overview of site looking to the northeast. The Cherchen He (CH) is in the right foreground, and the western stream (WS) incises the T1 surface. The T1/T2 riser is on the right side of the photograph. The arrows show the fault trace. (b) Typical quartz cobble embedded in the T1 surface. (c) The T0/T1 riser which was refreshed to obtain subsurface samples. The riser is 3–4 m high.

(western) ice stream north of the fault is 1020 ± 100 m (Figures 11d and 12b). Finally the two main postglacial streams that cross the till bench between the glaciers (labeled "S1" and "S2", Figure 12a) show sharp dogleg offsets on the fault of 500 ± 20 m and 460 ± 20 m, respectively.

## 3. Surface Dating

### 3.1. Analytical Approach

[12] The timing of surface abandonment was determined by radiocarbon dating (Table 1) and $^{10}$Be and $^{26}$Al cosmic ray surface exposure dating of both subsurface and partially embedded, surface quartz pebbles (Tables 2 and 3). All of the isotopic measurements, $^{14}$C, $^{10}$Be and $^{26}$Al, were made at the Center for Accelerator Mass Spectrometry at Lawrence Livermore National Laboratory. The radiocarbon data are calibrated after *Stuiver et al.* [1998], and the chemical separation methods for Be and Al follow *Kohl and Nishiizumi* [1992].

[13] Model ages for $^{10}$Be and $^{26}$Al were calculated using the following expression in which the concentration of the nuclide, $N$, is a function of the nuclide production rate at the surface, $P_0$, the exposure time, $t$, the depth below the surface, $z$, the decay constant (for radionuclides), $\lambda$, and the erosion rate, $\varepsilon$:

$$N(z,t) = \frac{P_0 e^{-\rho z/\Lambda}}{\lambda + \rho\varepsilon/\Lambda}\left(1 - e^{-(\lambda+\rho\varepsilon/\Lambda)t}\right), \quad (1)$$

where $\Lambda$ is the absorption mean free path and $\rho$ is the material density. For surface samples ($z = 0$) experiencing negligible erosion ($\varepsilon = 0$) this reduces to

$$N(0,t) = (P_0/\lambda)\left(1 - e^{-\lambda t}\right). \quad (2)$$

[14] The $^{10}$Be and $^{26}$Al production rates are based on the work by *Nishiizumi et al.* [1989] recalculated with the revised 13,000-year glacial retreat ages [*Clark et al.*, 1995] and rescaled for altitude and elevation [*Lal*, 1991]. Production rates were further modified to include the effects of a reduced muonogenic contribution of ~3% and a spallogenic contribution of 97% at sea level high latitude (SLHL) [*Owen et al.*, 2002]. Uncertainties on the concentrations include those from the procedural blank, carrier

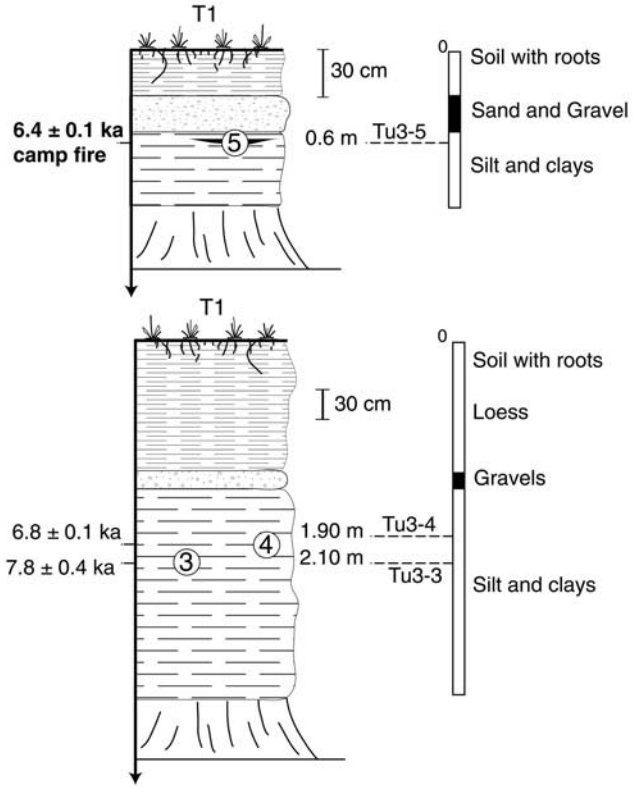


**Figure 5.** Sketch of the left-bank stream cut face of the T1 terrace of the eastern stream (ES) from which the charcoal samples were retrieved. All of the samples are located below the topmost level of gravels. Calibrated ages (ka) are indicated (INTERCAL'98 [*Stuiver et al.*, 1998]).

composition, and counting statistics. Errors on the model ages are calculated by propagating the analytical uncertainties together with a 6% error on the production rates [*Stone*, 2000] and 3.3% and 2.8% uncertainties for the decay constants of $^{10}$Be and $^{26}$Al, respectively [*Gosse and Phillips*, 2001]. To account for the decreased production rates at depth, the ages of subsurface samples are "depth-corrected" using equation (1) with $\rho = 2.1$ g/cm$^3$ and $\Lambda = 175$ g/cm$^2$. Errors are calculated as above and include additional uncertainties in density and attenuation length of 10%.

[15] The dates obtained by both $^{10}$Be and $^{26}$Al are reasonably consistent, but the $^{26}$Al ages appear to be systematically younger (Tables 1 and 3). We believe that this may be due to loss of volatile Al complexes during sample preparation. In general, we tend to have more confidence in the $^{10}$Be ages, as they require only one measurement $^{10}$Be/$^{9}$Be, while $^{26}$Al requires measurement of both $^{26}$Al/$^{27}$Al and Al concentration. In this paper we will discuss only the $^{10}$Be results. As $^{10}$Be ages are systematically older than the $^{26}$Al ones, using the $^{10}$Be alone will, holding all other factors constant, yield a relative minimum rate.

### 3.2. Results

#### 3.2.1. Cherchen He Site

[16] Surface cobbles were collected north and south of the fault on the T1 and T2 surfaces, and on T3 north of the fault. To evaluate the effects of predepositional inheritance on the cosmogenic ages [*Anderson et al.*, 1996; *Hancock et al.*, 1999], subsurface samples were also collected from the T1 terrace near WS (Figure 4c). For this we sampled two near vertical, free-faced risers cut by WS both up and downstream from the fault. Small charcoal fragments were retrieved near ES a few tens of centimeters below the uppermost sand and gravel layer beneath the surface of T1 (Figures 2 and 5).

[17] The three charcoal ages from the silt and clay from beneath the surface of T1 are in correct stratigraphic order, with ages ranging from 7.8 to 6.4 ka (Figure 5 and Table 1). None of these samples come from burrows or bioturbated sediments. Detrital charcoal samples often yield ages older than the age of deposition due to inclusion of an inherited

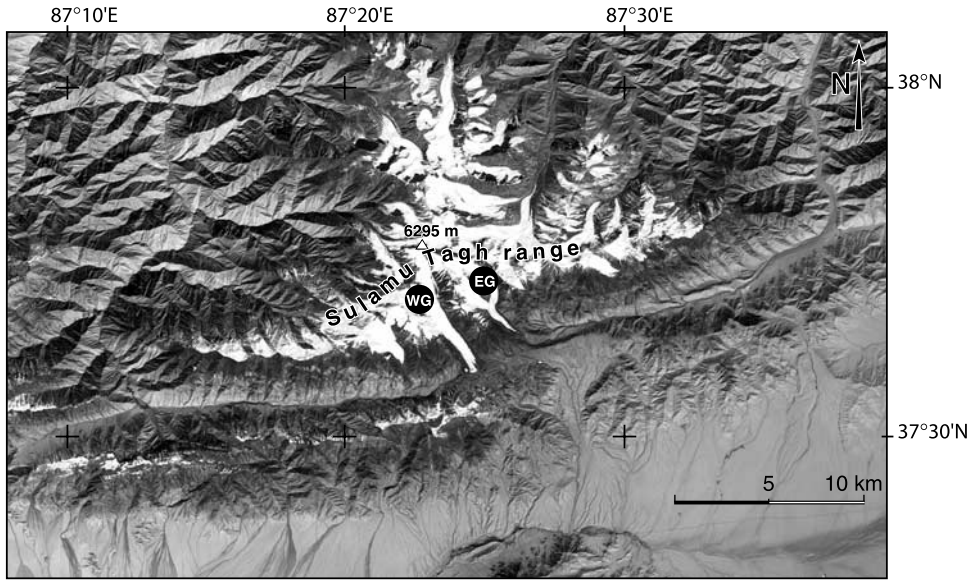


**Figure 6.** SPOT image (KJ 222-274) showing all the glaciers of the Sulamu Tagh massif. Western glacier (WG) and eastern glacier (EG) are the largest glaciers on the south flank of the range.

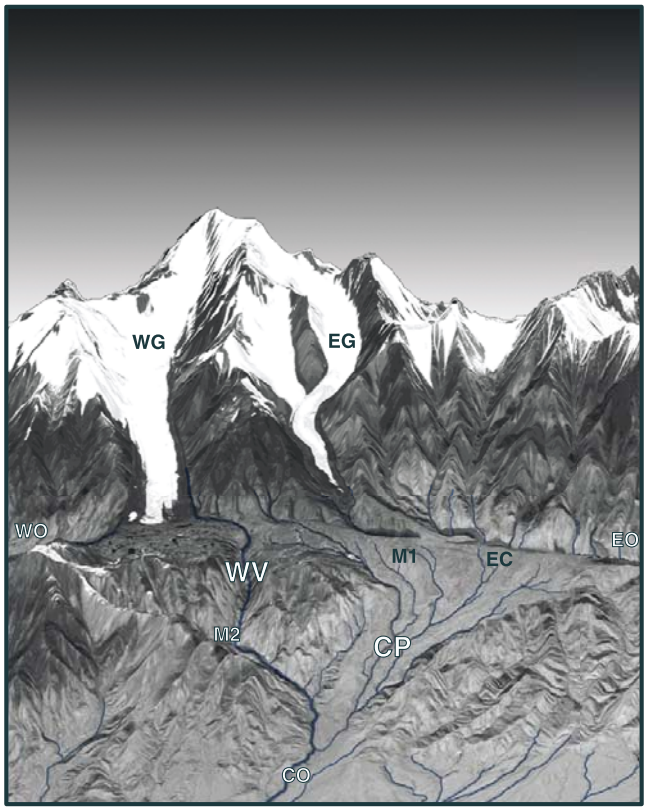


**Figure 7.** SPOT image draped on a digital elevation model of the Sulamu Tagh area processed from a digitized 1:100,000 scale Chinese map. WG and EG, west and east glaciers, respectively; WV, west paleoglacial valley; EC, east paleoglacial confluence; WO, CO, EO, west, central, and east glacial outwashes, respectively; M1, M2, youngest abandoned lateral moraines. The glacial confluence area (CP) abraded by glacial action is clearly smoother than the surrounding relief.

component. Here, however, the uppermost sample was collected in a burn lens that we interpret to be an in situ campfire, and therefore T1 must be younger than 6.4 ± 0.07 ka.

[18] The two $^{10}$Be depth profiles in T1 yield depth-corrected ages of subsurface samples (nine in total) ranging from as young as ~6 to 72 ka (Table 2). Depth-corrected ages of subsurface samples can only be perturbed from the true abandonment age by inheritance. The youngest subsurface samples therefore provide a maximum bound on the true abandonment age of the surface that, in turn, yields a minimum slip rate. The maximum age constraint provided by the youngest depth-corrected ages for T1, ~6 ka, is also in good agreement with the radiocarbon dating. Together these age estimates provide a strong argument for the abandonment of T1 at ~6 ka and also provides a basis for comparison with age estimates obtained from cosmogenic dating of surface samples.

[19] Age estimates from cosmogenic dating of surface materials can be influenced by predepositional inheritance, postdepositional contamination, erosion, and other surface processes that lead to mixing and turbation. The age distribution for surface and subsurface materials can therefore represent the amalgamation of more than one age population and can be further perturbed by surface processes. The observed distribution of ages therefore need not be normally distributed, or even unimodal. This is clearly demonstrated by the $^{10}$Be model ages from T1 surface. While this surface is rather firmly dated at ~6 ka based on radiocarbon dating, consistent with the youngest $^{10}$Be ages of subsurface samples, the 27 $^{10}$Be dates obtained (from both surface and subsurface cobbles) on T1 range from 3.55 to 72 ka (Table 2); the mean square weighted deviation (MSWD) is ~47 indicating that the sample cannot be drawn from a single, normally distributed population. Of the 27 samples, 12 fall within 2000 years of the radiocarbon/subsurface age estimate and only 2 samples yield ages that are significantly younger (TU3-59 and TU3-60; although as the radiocarbon age estimate is an upper bound on the surface age, these too may be in agreement). The remaining 15 samples are older than the radiocarbon age estimate by various amounts, and illustrate predepositional exposure inheritance, or diachronous deposition/abandonment as the predominant sources of error.

[20] Age clusters are often defined by visual rejection of outliers [*Van der Woerd et al.*, 2002b, 1998]. An established method for discarding outliers is Chauvenet's criterion which assesses the probability of finding a datum differing from the average by a given amount [see *Bevington and Robinson*, 2002, p. 58]. If the number of events expected at a certain value is less than some discriminant (typically 0.5 events), then that event can be discarded. The result of iterative application of this criterion to the T1 samples eliminates the 7 oldest ages from the population. The remaining 20 ages range from 3.7 to 11.6 ka (Figure 13). The simple average of the remaining data is 7.3 ± 2.2 ka (error is 1σ). While still not normally distributed (MSWD = 21.4), the 1σ error bracket calculated from the filtered data

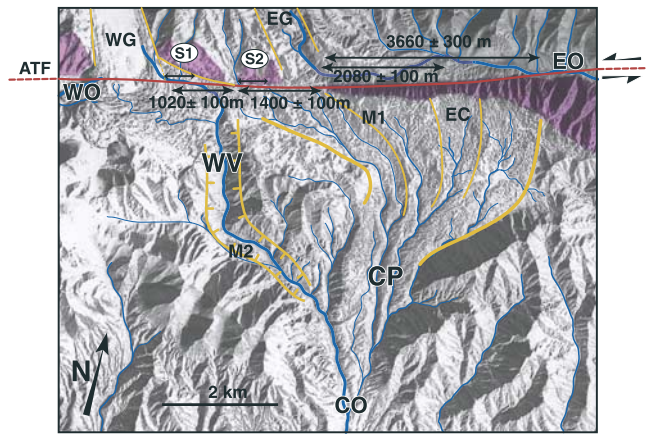


**Figure 8.** Map of glacial geomorphic features overlain on Corona image. The cumulative geomorphic scarp south of the fault (red line) and triangular facets north of ATF are shaded violet. Yellow lines (piercing lines) mark glacial channels or moraines. Cumulative offsets (in meters) are indicated. Numbers below arrows refer to offsets of eastern edge of WG. Numbers above the arrows are offsets relative to the eastern edge of EG. S1 and S2 indicate offset postglacial streams, with offsets of 500 ± 20 m and 460 ± 20 m, respectively.

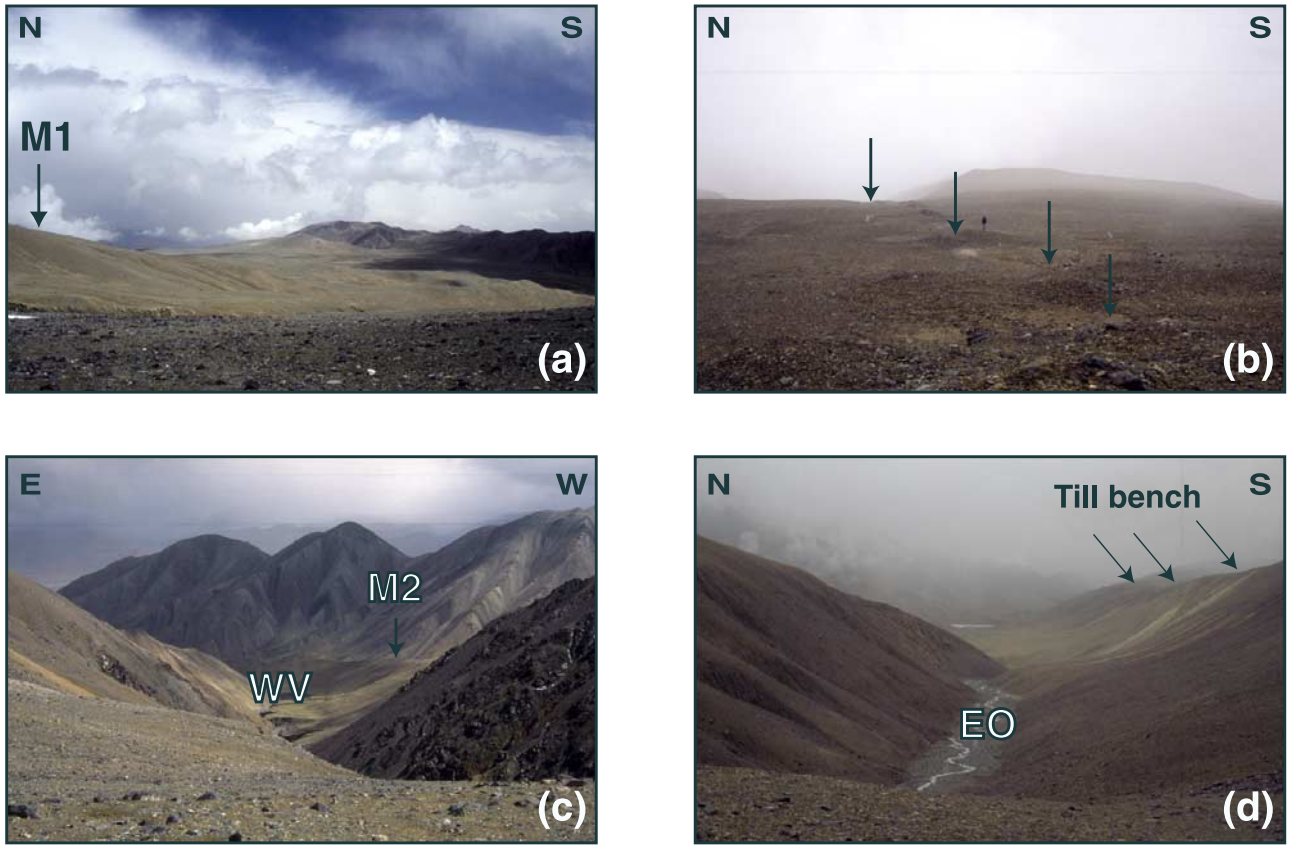


**Figure 9.** Sulamu Tagh site. (a) Overview of the paleoglacial confluence and more particularly the M1 moraine in the foreground; view to the northeast. (b) Fresh mole tracks and sag ponds on glacial till at Sulamu Tagh; view to the west. (c) Western valley WV and the youngest M2 moraine; view to the south. (d) Eastern outwash of EG. Note the 200-m-high till bench that isolates EO from CP; view to the east.

captures ~75% of the filtered data, as well as the radiocarbon age constraint of ~6 ka (Figure 13).

[21] Surface erosion can result in model ages that are younger than the true exposure age, but will not have a significant effect on samples as young as those on T1 (Figure 14). Postabandonment contamination of the surface can also perturb cosmogenic ages, but has no effect on subsurface radiocarbon ages. For T1, the agreement between radiocarbon ages and the youngest surface and subsurface cosmogenic ages demonstrates that erosion and postabandonment contamination have had negligible effect on the cosmogenic age determinations, and supports the use of zero-erosion rate model ages. On the basis of these three different age determinations, we conclude that T1 was abandoned no earlier than 7.3 ka and more likely after 6.4 ka as required by the uppermost charcoal age near ES.

[22] Only surface samples for cosmogenic dating were obtained from T2 (Table 2). Like those from T1, the 15 surface $^{10}$Be dates from T2 are not normally distributed (MSWD = 20.0), but are clearly older than the T1 samples ranging from 10.0 to 38.9 ka. In the absence of subsurface and/or radiocarbon ages, we have applied Chauvenet's criterion to filter the data, discarding the two oldest samples, TU3-64 and TU3-46, as outliers, likely influenced by predepositional exposure. The remaining 13 data range from 10.0 to 21.8 ka. The corresponding, unweighted average (and standard deviation) is 16.6 ± 3.9 ka. While again, not normally distributed (MSWD = 11.4) the 1σ error bracket does captures a majority of the data (Figure 13). Although we do not have other age constraints to compare with the surface samples, the similarity of the T1 and T2 surfaces' morphologies, lithologies and age distributions provides support for these error estimates. Hence we conclude that T2 was abandoned after 16.6 ± 3.9 ka. This average age, 16.6 ± 3.9 ka, includes the effects of diachronous emplacement/abandonment and inheritance. The final abandonment of T2 may be better approximated by the age of the youngest cobble, TU3-50, 10.0 ± 0.71 ka. Also, as is the case for T1, erosion has little effect on cosmogenic nuclide concentrations for samples of this age (Figure 14), and we use only model ages in the discussion.

[23] Three samples from the T3 surface yield ages between 72.3 and 91.6 ka (Table 2). The number of samples analyzed is too small to yield a robust age estimate. However, it is clear that T3 is considerably older than T1 and T2, confirming the correlation between surface height and relative age. In summary, the direct surface dating we performed supports the inference derived from geomorphic observation. The highest T3 remnant is oldest, and significantly predates the LGM. Both T1 and T2 postdate the LGM. The high-level fill terrace, T2, whose emplacement was likely due to deglaciation, is appreciably older than the

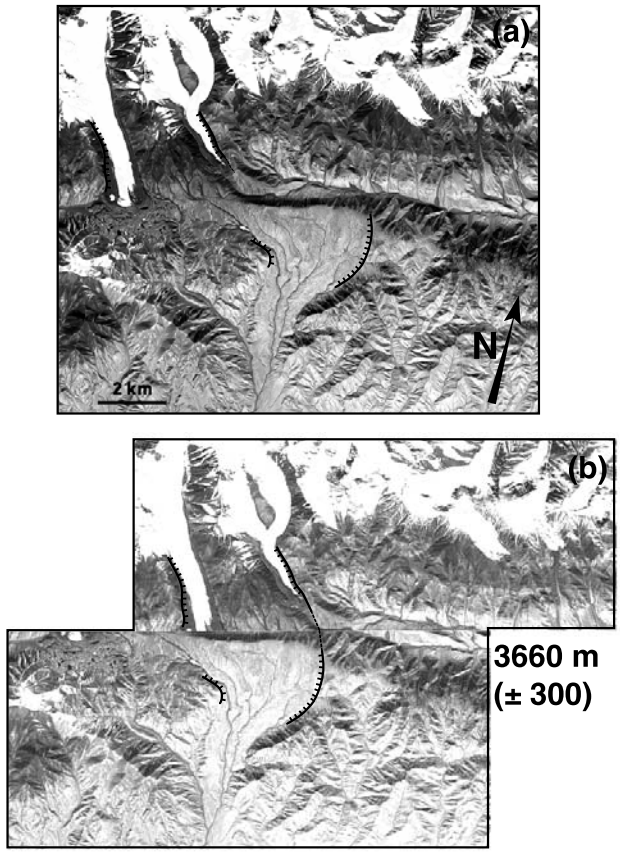


**Figure 10.** (a) Enlargement of the SPOT image at the Sulamu site. (b) Best fit of oldest, outer limits of glacial incision in CP with outer rims of EG and WG of 3660 ± 300 m.

lower T1 strath terrace, which formed during the Early Holocene Optimum.

#### 3.2.2. Sulamu Tagh Site

[24] Forty-four angular quartz cobbles collected along the crests of M1 and M2 and on the till bench, mostly south of the fault (Figure 15), were dated (Table 3). Three with discordant ages ($^{26}Al/^{10}Be$ model age <0.8) were discarded (NNM-15A, MHF-5, MHA-3). All the $^{10}Be$ model ages are younger than 113 ka (end of glacial stage 5d, Figure 15), implying that the Sulamu Tagh glaciers flooded the paleoglacial valley and confluence only during the last glacial cycle (Figure 15). The three oldest samples collected lie in the easternmost channel, near the eastern limit of glacial incision (Figure 15). The ages young to the west and the bulk of the till appears to have been emplaced between 80 and 40 ka (Table 3). The youngest ages (<38 ka) come from cobbles along the western paleoglacial valley (8 samples) and near the fault south of the eastern glacier (4 samples) (Figures 15 and 16 and Table 3). Among the former, the four samples that span roughly the period between the LGM and the onset of postglacial warming (23–13 ka) are from the crest of the geomorphically youngest moraine (M2), and on the eastern edge of WV south of the fault. Within the paleoglacial confluence, the next most sharply defined moraine, M1, shows fairly well clustered ages between 42 and 53 ka (Figures 15 and 16). Samples from the floor of EC, the deepest eastern channel of the paleoconfluence, show ages that cluster even more tightly between 64 and 68 ka (Figure 15). That the ages of distinct structures within the till complex increase eastward (Figure 16) is consistent with increasing sinistral offset of deposits fed by the same glacial sources on the Sulamu Tagh.

[25] At Cherchen He, the agreement between cosmogenic and radiocarbon dating of the surfaces insures that erosional effects on the age are insignificant. At Sulamu Tagh we do not have radiocarbon control and erosion may significantly perturb the model age for samples older than 50 ka (Figure 14). Neglecting the effect of erosion, which is to decrease the model age relative to the actual exposure age, would yield ages that are too young, and thus slip rates that are too high. In theory, the $^{26}Al/^{10}Be$ ratio can be used to constrain erosion rates. However, this is only the case for very old samples with negligible erosion rates [*Bierman and Caffee*, 2001; *Nishiizumi et al.*, 1991]. Erosion has an effect similar to increasing the decay constant and samples experiencing rapid erosion reach steady state before the $^{26}Al/^{10}Be$ ratio can deviate from the production ratio (equation (1)). As a result, erosion rates are difficult to constrain using only $^{10}Be$-$^{26}Al$ systematics. The effect erosion might have on model ages characteristic of the Sulamu Tagh site is shown in Figure 14 and is most pronounced for the ~113 ka samples from the eastern edge of the confluence and the ~65 ka samples from EC (Figure 15). For instance, an erosion rate of 8 m/Myr would yield a zero erosion rate model age of ~66 ka for a sample with a true exposure age of ~100 ka. Similarly, a rate of 6 m/Myr would reduce the model age of a ~250 ka sample to ~110 ka. These erosion rates are similar to the maximum mean, alpine bedrock summit erosion rate, 7.6 ± 3.9 m/Myr, determined for four ranges in the western United States [*Small et al.*, 1997]. Erosion should also lead to dispersion of model ages if its rate was spatially variable. Here the lack of dispersion among the model ages from EC and M1 argues that erosion may not have significantly perturbed the exposure ages within the paleoconfluence.

[26] Arguing against significant erosion is the observation that the surface of the confluence is relatively flat with much lower topographic gradient and roughness than the surrounding bedrock surfaces (Figures 6 and 7). It is protected from high-powered streams flowing from the north by the steep valley wall along the fault trace and hosts only small catchments. However, it is also clear that the surfaces have not maintained their original depositional morphology, relative to the younger moraines at the terminus of the western glacier, and some postdepositional surface smoothing must be accepted. The offset-age relationships for the eastern edge of the paleoconfluence and the eastern channel, EC, play an important role in extracting slip rate information from this site. Therefore, while it is not common practice to correct surface ages for the effects of erosion, it is prudent, given the absence of constraints on erosion rates, to consider more conservative age-offset relationships that do not rely solely on zero erosion rate model ages.

## 4. Discussion

### 4.1. Effects of Climate on Landscape Evolution

[27] It is generally appreciated that landscape evolution is moderated by climate change [e.g., *Bull*, 1991]. The mor-

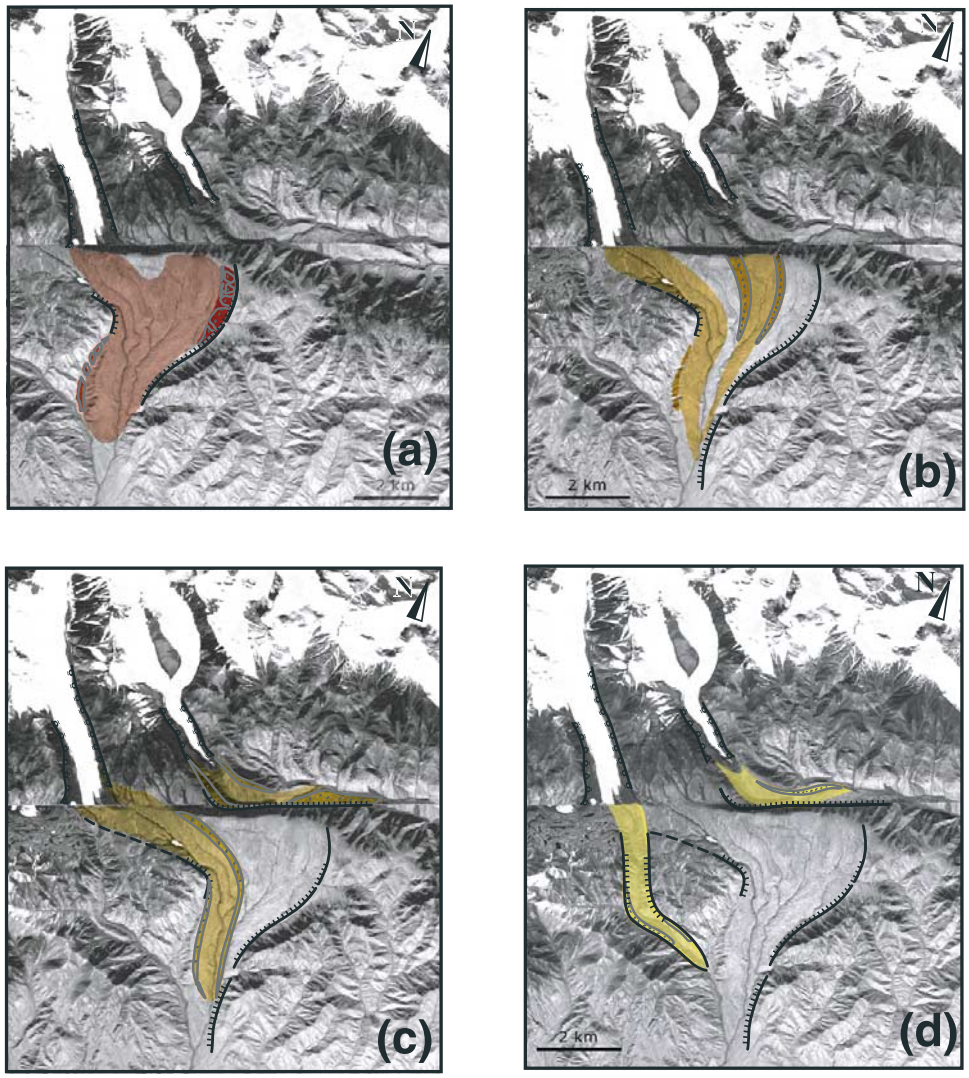


**Figure 11.** Restored offsets of WV, M1, EC and CP at Sulamu Tagh. Corresponding epochs and amounts of back slip on ATF are (a) 3660 ± 300 m since ~112 ka, (b) 2080 ± 100 m since ~66 ka, (c) 1400 ± 100 m since ~47 ka, and (d) 1020 ± 100 m since ~34 ka. Major diversion of glacial ice streams probably occurred on occasion of ~55 and ~35 ka interstadials.

phochronological data presented here provide an opportunity to quantitatively assess the link between landscape evolution and climate in northern central Tibet. Geographically the closest available paleotemperature record is the ~130 kyr, $\delta^{18}O$ record from the Guliya ice cap of the western Kunlun [*Thompson et al.*, 1997]. The surface exposure ages of both glacial and fluvial features adjacent to the Sulamu Range are generally compatible with the cycle of glaciations observed in that $\delta^{18}O$ record (Figure 17). The sharp ~112 ka drop in $\delta^{18}O$ at Guliya coincides with the oldest ages obtained on the eastern margin of the paleoglacial confluence at Sulamu Tagh, 112.7 ± 7.3 ka (oldest sample from CP, NNM-68, Figures 15 and 17), supporting the inference that the confluence began to be shaped when invaded by the inflated glaciers as the climate cooled at the beginning of marine isotope stage (MIS) 5d. The other distinct age clusters within the confluence (66 ± 1.8 ka and 47 ± 4 ka) lie within the ice cap $\delta^{18}O$ minima of MIS-4 and MIS-3 and are separated by the interstadial at 55 ± 5 ka (Figure 17). The M1 moraine was probably emplaced by the western glacier at the climax of MIS-3. During that stage, the eastern glacier, which had likely withdrawn north of the fault during the 55 ka interstadial, advanced along a new path, deviating eastward along the fault, and cutting the north facing NE boundary of the till bench (Figures 9d and 11). In turn, the western channel of the confluence (WC) was likely abandoned as the western glacier retreated during the 37 ± 3 ka interstadial (Figures 11 and 15). The western glacier then readvanced, straight down slope across the fault, carving the western valley, as the climate cooled again after that interstadial, and during MIS-2 (32 ± 2 ka). Finally, streams 1 and 2 could not have incised their present channels until the bench was free of ice (Figure 12). Hence they probably started to incise narrow channels into the till at the beginning of the pluvial following the onset of postglacial warming around 15 ± 3 ka. This would be in keeping with the ~16.5 ka age of the highest fill terrace (T2) at the Cherchen He site (Figures 2

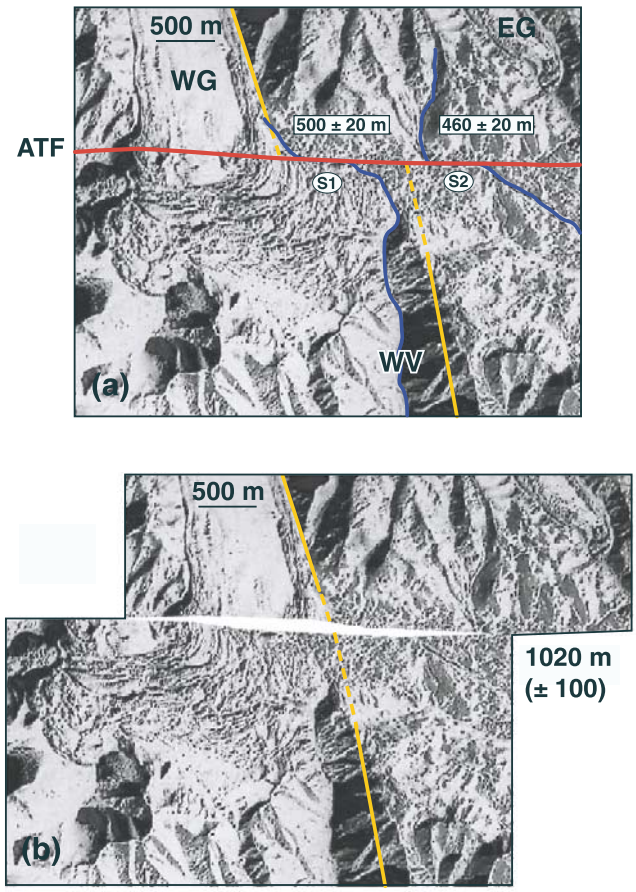


**Figure 12.** (a) Enlargement of Corona image of the Sulamu Tagh site. (b) Best fit of the eastern edge of WV and WG of 1020 ± 100 m. The two postglacial streams denoted by S1 and S2 are offset 500 ± 20 and 460 ± 20 m, respectively.

and 13). The western glacier concurrently retreated to its present, ponded position, with one lobe already veering into the western outwash valley (WO).

[28] The surfaces at the Cherchen He site record a smaller time interval than those at the Sulamu Tagh site, but the imprint of climate change on landscape evolution is evident. Based upon the Guliya ice cap paleoclimatic record (western Kunlun, Figures 1 and 17), the LGM in this area has been estimated to be ~18.5 ka [*Thompson et al.*, 1997]. The majority of the cosmogenic ages from T2 are younger than 18.5 kyr, and the older samples can be easily explained by inherited components. It has been suggested that fluvial terraces of similar age along the northern side of the Tien Shan were deposited after the LGM when catchments were rich in glacial debris, and stream power was high [*Poisson*, 2002; *Poisson and Avouac*, 2004]. Others have suggested that terrace deposition most likely takes place during glacial maxima due to high sediment supply as a result of active glacial erosion [e.g., *Molnar et al.*, 1994]. Here, the temporal constraints clearly demonstrate that T2 was abandoned well after the LGM. Hence the emplacement of this terrace would appear to have coincided with post LGM deglaciation when high stream power in short, steep catchments could most efficiently flush debris.

[29] The abandonment of T1, at ~6 ka, occurs during the Holocene interstadial and is closely associated with the end of the early Holocene Optimum. Pollen distributions and other indicators in lacustrine core samples from Sumxi Co, in NW Tibet, indicate humid conditions from 9 to 6 ka in the region, decreasing abruptly at 6–5 ka [*Gasse et al.*, 1991], within error of the age of T1 (Figures 13 and 17). The abandonment of T1 at ~6 ka may thus have been a response to decreased stream power and sediment load due to the onset of more arid conditions. The river may no longer have been able to maintain a broad, aggrading bed, resulting in incision and abandonment. *Ryerson et al.* [1999] and *Van der Woerd et al.* [1998, 2000, 2002b] have dated terraces with similar cosmic ray exposure ages along the Karakax Valley Fault (78°E) and Kunlun Fault, respectively, suggesting that this change in moisture supply was a regional, north Tibetan event, affecting most hydrologic systems and reflected in the history of landscape evolution.

### 4.2. Slip Rates

[30] Morphologic offsets and exposure ages can be combined to yield millennial slip rates on the ATF. The T2/T1 riser at Cherchen He most likely started to record cumulative displacement when T1 was abandoned, as demonstrated at similar fluvial sites along the Kunlun Fault by *Van der Woerd et al.* [1998, 2000, 2002b]. The age of this surface is best constrained by radiocarbon dating (<6.4 ± 0.07 ka), supported by $^{10}$Be dating of subsurface samples (≥6.0 ± 0.38 ka). Combining the 166 ± 10 m offset of T2/T1 (Figure 2) with the radiocarbon constraint yields a slip rate of 25.9 ± 1.6 mm/yr. Similarly linking the radiocarbon age with the 180 m offset of T2/T1 near ES (Figure 2) yields a rate of 28.1 ± 1.6 mm/yr. Including the 1σ error brackets from both these offsets we bracket the slip rate between 24.3 and 29.7 mm/yr (equivalent to 27.0 ± 2.7 mm/yr, Figure 18a). Linking the two T2/T1 offsets with the average $^{10}$Be age of T1, 7.3 ± 2.2 ka, yields somewhat less precise rates of 22.7 ± 6.9 mm/yr and 24.6 ± 7.5 mm/yr for the 166 m and 180 m offsets, respectively. With the exception of two very high rates (TU3-60 and TU3-59), the error brackets obtained from the average $^{10}$Be age of T1 captures all of the rates obtained by propagating the ages of the individual samples (Figure 18a). That a number of these

**Table 1.** Calibrated Radiocarbon Ages of Charcoals Collected in T1 at Cherchen Site

| Sample | Depth, m | $\delta^{13}C$ | Fraction Modern | $\Delta^{14}C$ | $^{14}C$ Age, years | Calibrated Age,[a] years B.P. |
|---|---|---|---|---|---|---|
| TU3-98-3 | 2.1 | −25 | 0.4218 ± 0.0211 | −578.2 ± 21.1 | 6940 ± 410 | 7800 ± 410 |
| TU3-98-4 | 1.9 | −25 | 0.4759 ± 0.0048 | −524.1 ± 4.8 | 5970 ± 90 | 6786 ± 110 |
| TU3−98-5 | 0.6 | −25 | 0.4976 ± 0.0034 | −502.4 ± 3.4 | 5610 ± 60 | 6377 ± 70 |

[a]From *Stuiver et al.* [1998].

**Table 2.** $^{10}$Be and $^{26}$Al Surface Exposure Ages From the Cherchen He Site

| Sample | Measured $^{10}$Be,[a] $10^6$ atoms/g $SiO_2$ | Measured $^{26}$Al,[a] $10^6$ atoms/g $SiO_2$ | Depth,[b] cm | $^{10}$Be Model Age,[c] kyr | $^{26}$Al Model Age,[c] kyr |
|---|---|---|---|---|---|
| | | *T1 South* | | | |
| TU3-1 | 0.322 ± 0.011 | 1.870 ± 0.095 | 0 (1) | 7.35 ± 0.51 | 7.13 ± 0.56 |
| TU3-4 | 0.276 ± 0.009 | 1.454 ± 0.102 | 0 (1) | 6.30 ± 0.43 | 5.53 ± 0.51 |
| TU3-5 | 0.631 ± 0.018 | 3.354 ± 0.131 | 0 (1) | 14.48 ± 0.96 | 12.87 ± 0.93 |
| TU3-7 | 1.421 ± 0.042 | 7.385 ± 0.219 | 0 (1) | 32.63 ± 2.20 | 28.45 ± 1.93 |
| TU3-9 | 0.269 ± 0.017 | 1.410 ± 0.077 | 0 (1) | 6.14 ± 0.53 | 5.38 ± 0.44 |
| TU3-6 | 0.231 ± 0.007 | 1.371 ± 0.090 | 0 (1) | 5.30 ± 0.36 | 5.24 ± 0.47 |
| TU3-8 | 0.304 ± 0.009 | 1.671 ± 0.093 | 0 (1) | 6.92 ± 0.46 | 6.35 ± 0.52 |
| TU3-11 | 0.483 ± 0.016 | 2.234 ± 0.100 | 0 (1) | 11.07 ± 0.75 | 8.56 ± 0.64 |
| TU3-13 | 0.410 ± 0.015 | 1.986 ± 0.079 | 0 (1) | 9.36 ± 0.66 | 7.57 ± 0.55 |
| TU3-14 | 0.618 ± 0.016 | 3.385 ± 0.101 | 0 (1) | 14.10 ± 0.92 | 12.92 ± 0.87 |
| TU3-15 | 0.252 ± 0.015 | 1.314 ± 0.082 | 0 (1) | 5.75 ± 0.48 | 5.00 ± 0.43 |
| TU3-16 | 0.248 ± 0.009 | 1.420 ± 0.061 | 0 (1) | 5.64 ± 0.40 | 5.40 ± 0.40 |
| TU3-18 | 0.354 ± 0.013 | 1.976 ± 0.169 | 12.5 (0.80) | 10.05 ± 0.66 | 9.37 ± 0.85 |
| TU3-19 | 0.281 ± 0.006 | 1.601 ± 0.063 | 20.0 (0.72) | 8.9 4 ± 0.55 | 8.52 ± 0.56 |
| TU3-20 | 0.189 ± 0.004 | 1.042 ± 0.071 | 22.5 (0.68) | 6.31 ± 0.38 | 5.82 ± 0.44 |
| TU3-21 | 0.167 ± 0.006 | 0.909 ± 0.036 | 27.5 (0.63) | 6.04 ± 0.38 | 5.50 ± 0.35 |
| TU3-22 | 0.266 ± 0.007 | 1.562 ± 0.056 | 47.5 (0.46) | 13.27 ± 0.81 | 12.99 ± 0.81 |
| TU3-24 | 0.836 ± 0.016 | 4.882 ± 0.322 | 42.5 (0.50) | 38.62 ± 2.34 | 37.77 ± 2.62 |
| TU3-25 | 0.166 ± 0.005 | 0.899 ± 0.118 | 50.0 (0.44) | 8.54 ± 0.52 | 7.70 ± 0.65 |
| | | *T1 North* | | | |
| TU3-57 | 0.369 ± 0.019 | 2.001 ± 0.085 | 0 (1) | 8.24 ± 0.65 | 7.47 ± 0.55 |
| TU3-58 | 0.516 ± 0.019 | 2.481 ± 0.084 | 0 (1) | 11.57 ± 0.82 | 9.28 ± 0.64 |
| TU3-59 | 0.219 ± 0.016 | 0.965 ± 0.046 | 0 (1) | 4.91 ± 0.46 | 3.60 ± 0.28 |
| TU3-60 | 0.165 ± 0.014 | 1.084 ± 0.095 | 0 (1) | 3.70 ± 0.38 | 4.05 ± 0.43 |
| TU3-61 | 1.173 ± 0.034 | 5.954 ± 0.190 | 0 (1) | 26.44 ± 1.78 | 22.48 ± 1.54 |
| TU3-62 | 0.237 ± 0.015 | 1.350 ± 0.061 | 0 (1) | 5.31 ± 0.46 | 5.06 ± 0.38 |
| TU3-70 | 0.284 ± 0.006 | 1.562 ± 0.107 | 25.0 (0.66) | 9.67 ± 0.59 | 8.87 ± 0.66 |
| TU3-71 | 0.893 ± 0.017 | 4.780 ± 0.159 | 80.0 (0.28) | 71.80 ± 4.55 | 64.32 ± 4.22 |
| | | *T2 South* | | | |
| TU3-42 | 0.613 ± 0.021 | 4.107 ± 0.169 | 0 (1) | 13.88 ± 0.96 | 15.56 ± 1.14 |
| TU3-43 | 1.004 ± 0.165 | 3.708 ± 0.155 | 0 (1) | 22.76 ± 4.00 | 14.03 ± 1.03 |
| TU3-45 | 0.962 ± 0.026 | 5.071 ± 0.165 | 0 (1) | 21.82 ± 1.44 | 19.27 ± 1.33 |
| TU3-46 | 1.130 ± 0.022 | 6.216 ± 0.256 | 0 (1) | 25.67 ± 1.63 | 23.68 ± 1.74 |
| TU3-47 | 0.819 ± 0.021 | 3.326 ± 0.115 | 0 (1) | 18.59 ± 1.22 | 12.60 ± 0.88 |
| TU3-48 | 0.588 ± 0.016 | 2.956 ± 0.129 | 0 (1) | 13.32 ± 0.88 | 11.20 ± 0.84 |
| TU3-49 | 0.801 ± 0.028 | 4.310 ± 0.185 | 0 (1) | 18.18 ± 1.26 | 16.37 ± 1.22 |
| TU3-50 | 0.440 ± 0.017 | 2.643 ± 0.079 | 0 (1) | 10.00 ± 0.71 | 10.04 ± 0.68 |
| TU3-51 | 0.774 ± 0.024 | 4.344 ± 0.298 | 0 (1) | 17.59 ± 1.19 | 16.52 ± 1.52 |
| TU3-52 | 0.711 ± 0.022 | 4.163 ± 0.150 | 0 (1) | 16.18 ± 1.09 | 15.85 ± 1.12 |
| | | *T2 North* | | | |
| TU3-63 | 0.553 ± 0.014 | 2.693 ± 0.088 | 0 (1) | 12.36 ± 0.81 | 10.05 ± 0.69 |
| TU3-64 | 1.771 ± 0.035 | 9.606 ± 0.266 | 0 (1) | 39.89 ± 2.54 | 36.39 ± 2.45 |
| TU3-65 | 0.596 ± 0.018 | 3.841 ± 0.177 | 0 (1) | 13.31 ± 0.89 | 14.36 ± 1.09 |
| TU3-67 | 0.746 ± 0.018 | 3.974 ± 3.835 | 0 (1) | 16.65 ± 1.08 | 14.83 ± 14.45 |
| TU3-69 | 0.942 ± 0.019 | 4.966 ± 0.142 | 0 (1) | 21.06 ± 1.34 | 18.59 ± 1.25 |
| | | *T3 North* | | | |
| TU3-53 | 3.147 ± 0.067 | 20.088 ± 0.848 | 0 (1) | 72.25 ± 4.68 | 78.58 ± 5.99 |
| TU3-55 | 4.026 ± 0.083 | 15.396 ± 0.582 | 0 (1) | 91.64 ± 5.94 | 58.87 ± 4.30 |
| TU3-56 | 3.591 ± 0.061 | 19.019 ± 0.143 | 0 (1) | 81.56 ± 5.18 | 73.24 ± 4.59 |

[a]Propagated analytical uncertainties include error blank, carrier and counting statistics.

[b]Depth correction beneath flat surface, in parentheses, has been calculated considering attenuation of flux coming from all azimuthal directions, where intensity of flux at depth is $I(x) = I(0)\exp(-\mu L(x))$, attenuation is $\mu = \rho/\Lambda$, and distance through matter is $L(x) = x/\sin(\theta)$, $\theta$ being inclination of incoming radiation. A density $\rho = 2.1$ g/cm$^3$ and attenuation length $\Lambda = 175$ g/cm$^2$ have been used.

[c]"Zero erosion" model ages are calculated with propagated analytical uncertainties including 6% uncertainty on production rate [*Stone*, 2000], and 3.3 and 2.8% uncertainties for decay constants of $^{10}$Be and $^{26}$Al, respectively [*Gosse and Phillips*, 2001], as well as uncertainty of 10% on density and attenuation length for depth samples.

individually propagated rates are lower than that obtained from the radiocarbon age is likely a result of inheritance and/or diachronous emplacement/abandonment of T1.

[31] A minimum estimate of the slip rate can be obtained by assuming that T1 is a fill terrace and that the T2/T1 offset predates its deposition. In this model, the age of the T2/T1 offset is given by the minimum age of the upper terrace, T2, as a riser cannot predate the final abandonment of the terrace into which it is incised. As the youngest cobble on T2 is 10 ± 0.71 ka (TU3-50, Table 2) we obtain minimum rate estimates of 16.6 ± 1.5 and 18 ± 2.4 mm/yr, respectively, for the 166- and 180-m offsets of T2/T1. We stress, however, that these minimum rates are in conflict with the key geomorphic observation that T1 is a strath terrace that

**Table 3.** Cosmogenic $^{10}$Be and $^{26}$Al Dating Results From the Sulamu Tagh

| Sample | Measured $^{10}$Be,[a] $10^6$ atoms/g $SiO_2$ | Measured $^{26}$Al,[a] $10^6$ atoms/g $SiO_2$ | $^{10}$Be Model Age,[b] kyr | $^{26}$Al Model Age,[b] kyr |
|---|---|---|---|---|
| NNM-13A | 4.023 ± 0.157 | 21.014 ± 0.859 | 38.2 ± 2.8 | 33.5 ± 2.5 |
| NNM-15A | 0.398 ± 0.028 | 1.793 ± 0.123 | 4.2 ± 0.4 | 3.2 ± 0.3 |
| NNM-14A | 1.597 ± 0.060 | 7.524 ± 0.273 | 17.0 ± 1.2 | 13.4 ± 0.9 |
| NNM-16A | 0.398 ± 0.021 | 1.999 ± 0.104 | 4.2 ± 0.3 | 3.5 ± 0.3 |
| NNM-17A | 1.682 ± 0.051 | 8.561 ± 0.365 | 18.0 ± 1.2 | 15.3 ± 1.1 |
| NNM-18A | 7.139 ± 0.307 | 37.750 ± 1.469 | 77.2 ± 5.8 | 69.2 ± 5.1 |
| NNM-11A | 7.900 ± 0.158 | 43.732 ± 1.202 | 76.3 ± 4.9 | 71.6 ± 4.9 |
| NNM-10A | 4.739 ± 0.258 | 24.519 ± 1.198 | 45.0 ± 3.7 | 39.2 ± 3.1 |
| NNM-12A | 5.160 ± 0.146 | 25.100 ± 5.040 | 49.2 ± 3.3 | 40.2 ± 8.6 |
| NNM-5 | 1.518 ± 0.059 | 8.628 ± 0.218 | 13.0 ± 0.9 | 12.4 ± 0.8 |
| NNM-6 | 2.706 ± 0.068 | 14.262 ± 0.410 | 23.3 ± 1.5 | 20.6 ± 1.4 |
| NNM-7 | 3.730 ± 0.121 | 21.538 ± 0.577 | 31.4 ± 2.2 | 30.4 ± 2.0 |
| NNM-1 | 4.384 ± 0.091 | 23.346 ± 0.697 | 37.4 ± 2.4 | 33.5 ± 2.3 |
| NNM-2 | 5.964 ± 0.158 | 30.031 ± 0.898 | 51.0 ± 3.4 | 43.2 ± 3.0 |
| NNM-4 | 4.884 ± 0.099 | 26.095 ± 1.051 | 41.6 ± 2.7 | 37.4 ± 2.7 |
| NNM-3 | 4.661 ± 0.141 | 26.826 ± 0.737 | 39.8 ± 2.7 | 38.5 ± 2.6 |
| NNM-8 | 3.936 ± 0.105 | 20.381 ± 0.843 | 34.7 ± 2.3 | 30.2 ± 2.2 |
| NNM-9 | 10.153 ± 0.260 | 51.290 ± 2.530 | 92.6 ± 6.2 | 79.4 ± 6.4 |
| NNM-10R | 2.704 ± 0.070 | 14.083 ± 0.685 | 23.8 ± 1.6 | 20.8 ± 1.6 |
| MF3/RR-1 | 4.610 ± 0.228 | 25.300 ± 0.211 | 45.1 ± 3.5 | 41.7 ± 2.6 |
| MF3/RR-2° | 5.050 ± 0.075 | 27.700 ± 0.037 | 49.5 ± 3.1 | 45.7 ± 2.8 |
| MF3/RR-3 | 4.254 ± 0.114 | 23.558 ± 1.060 | 41.6 ± 2.8 | 38.7 ± 3.0 |
| MF3/RR-4 | 5.435 ± 0.136 | 28.765 ± 0.721 | 53.3 ± 3.5 | 47.5 ± 3.2 |
| MF/RR-5 | 4.675 ± 0.117 | 25.784 ± 0.910 | 45.7 ± 3.0 | 42.5 ± 3.0 |
| NNM-30 | 6.750 ± 0.131 | 37.215 ± 1.501 | 65.0 ± 4.2 | 60.6 ± 4.5 |
| NNM-32 | 6.695 ± 0.168 | 35.453 ± 1.301 | 64.4 ± 4.3 | 57.6 ± 4.2 |
| NNM-31 | 7.032 ± 0.175 | 36.673 ± 1.091 | 67.7 ± 4.5 | 59.7 ± 4.1 |
| NNM-33 | 7.054 ± 0.141 | 35.959 ± 1.069 | 68.0 ± 4.4 | 58.5 ± 4.0 |
| NNM-34 | 9.015 ± 0.230 | 48.171 ± 1.438 | 91.0 ± 6.1 | 82.6 ± 5.8 |
| NNM-67 | 11.000 ± 0.598 | 61.254 ± 2.030 | 111.5 ± 9.3 | 106.3 ± 7.7 |
| NNM-68 | 11.109 ± 0.210 | 61.063 ± 1.376 | 112.7 ± 7.3 | 105.9 ± 7.2 |
| NNM-70 | 5.606 ± 0.156 | 31.252 ± 0.907 | 56.1 ± 3.8 | 52.8 ± 3.6 |
| NNM-71 | 5.573 ± 0.106 | 30.935 ± 0.697 | 55.8 ± 3.6 | 52.3 ± 3.4 |
| MHF-1 | 4.889 ± 0.092 | 23.793 ± 0.788 | 44.4 ± 2.8 | 36.3 ± 2.5 |
| MHF-4 | 0.736 ± 0.183 | 3.796 ± 0.146 | 6.6 ± 1.7 | 5.7 ± 0.4 |
| MHF-2 | 3.801 ± 0.127 | 20.248 ± 0.649 | 34.5 ± 2.4 | 30.8 ± 2.1 |
| MHF-3 | 5.883 ± 0.084 | 32.073 ± 1.367 | 53.6 ± 3.3 | 49.3 ± 3.7 |
| MHF-5 | 0.579 ± 0.025 | 2.097 ± 0.083 | 5.2 ± 0.4 | 3.2 ± 0.2 |
| MHAS-1 | 7.524 ± 0.190 | 36.758 ± 1.019 | 68.8 ± 4.6 | 56.7 ± 3.9 |
| MHAS-2 | 9.205 ± 0.177 | 44.612 ± 1.217 | 84.5 ± 5.4 | 69.2 ± 4.7 |
| MHAS-3 | 10.834 ± 0.211 | 3.073 ± 0.101 | 99.8 ± 6.4 | 4.6 ± 0.3 |
| MHAS-4 | 5.821 ± 0.080 | 32.708 ± 1.181 | 53.0 ± 3.3 | 50.3 ± 3.6 |
| MHAS-5 | 5.915 ± 0.074 | 33.662 ± 1.222 | 53.9 ± 3.3 | 51.8 ± 3.7 |
| MHAS-6 | 8.414 ± 0.155 | 42.249 ± 1.387 | 77.1 ± 4.9 | 65.4 ± 4.6 |

[a]Propagated analytical uncertainties include error blank, carrier and counting statistics.
[b]Zero erosion model ages are calculated with propagated analytical uncertainties including 6% uncertainty on production rate [*Stone*, 2000], and 3.3 and 2.8% uncertainties for decay constants of $^{10}$Be and $^{26}$Al, respectively [*Gosse and Phillips*, 2001].

cut the T2/T1 riser, rather than a fill terrace that would have flooded a more ancient channel dug into the T2 conglomerates, without altering the shape and position of the corresponding T2/T1 riser.

[32] The 418 ± 20 m offset of channel PC into T2 provides another minimum estimate of the slip rate, as the channel must postdate the abandonment of the surface into which it is incised. This is true regardless of whether T2 itself is a strath or fill terrace. The rates obtained by propagating the errors from 13 ''accepted'' surface dates (Figure 13) range from ~18 to 42 mm/yr (Figure 18b). Eliminating the highest rate (TU-50, as it approaches that of current Indo-Asian convergence and is likely the result of postdepositional contamination) we obtain a bracket of 18–34 mm/yr, close to that obtained from propagation of the unweighted average age and standard deviation of T2 (16.6. ± 3.9 ka, Figure 13), 25.2 ± 5.9 mm/yr, and compatible with the rate obtained from the T2/T1 offset (Figure 18). The absolute minimum bound, 18.4 ± 3.3 mm/yr, is obtained from the oldest $^{10}$Be age on T2 and is comparable to the minimum rate obtained from the ''fill'' terrace interpretation of the age of T2/T1 above.

[33] At the Sulamu Tagh site, the climatically governed timing of glacial advance and retreat constrains the history of cumulative offsets by the fault. The rates determined are somewhat less robust than those from Cherchen He owing to the paucity of cosmogenic dates north of the fault. In addition, no radiocarbon dates were obtained at Sulamu Tagh, making it more difficult to constrain the effects of erosion on the older cosmogenic ages. These uncertainties must be considered in establishing bounds on the slip rate.

[34] The key stages illustrating the interplay between fault movement and glacial or postglacial deposition and/or incision are shown in the reconstruction of Figure 11, and the ages of the offsets are given in Table 4. The oldest offset that can be constrained (3660 ± 300 m) is that of the outer

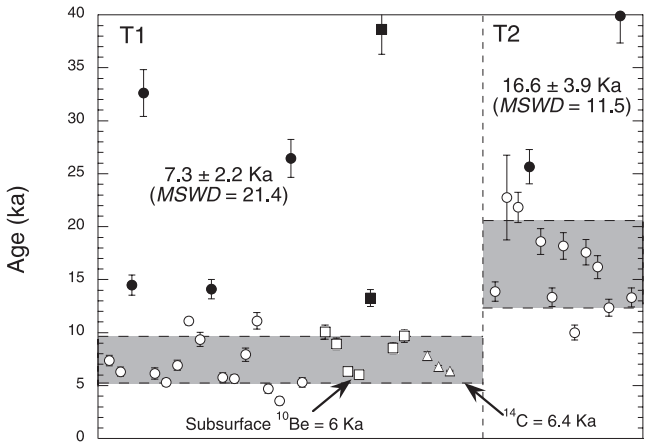


**Figure 13.** The $^{10}$Be exposure model age determinations at Cherchen He. The average values are a simple unweighted means with errors equal to one standard deviation for surface samples. The 1σ brackets on the average ages are shown as the shaded regions. The $^{10}$Be ages of samples included in the average are shown as open symbols; solid symbols are for ages that were rejected (see text). Surface samples are shown as open and solid circles, and depth-corrected ages of subsurface samples are shown as open and solid squares. Radiocarbon ages are shown as open triangles. Surface samples yield an average age of 7.3 ± 2.2 ka for T1 and an average of 16.6 ± 3.9 ka for T2. Sample TU3-71, 71.8 ± 4.6 ka, has not been plotted in order to improve the resolution in the age range of interest.

edges of the broad paleoconfluence relative to the positions of the active glaciers WG and EG which, given the absence of other large glaciers north of the fault (Figure 6), represent the only plausible source for the paleoconfluence. Cosmogenic dating and climatic correlations indicate that excavation of the paleoconfluence likely began at 112.7 ± 7.3 ka at the end of the last interglacial (MIS-5e). This yields a slip rate of 32.5 ± 3.4 mm/yr. As discussed earlier, however, erosion is not easily constrained at this site, and model ages may yield a minimum estimate of the age. While there is no local climate proxy that extends beyond ~130 ka, the previous two major cooling cycles from the global SPECMAP record are between 170–150 ka (MIS-6) and 200–180 ka (MIS-7) [*Imbrie et al.*, 1984; *Winograd et al.*, 1997]. That glacial advance associated with these older cooling events could have produced the observed features provides an alternative to our proposed model. These older advances would yield slip rates of 20.9–24.4 mm/yr and 18.3–20.3 mm/yr, respectively, in broad agreement with the minimum slip rates determined from the 166 m offset at the Cherchen He site. While both values are lower than the rate obtained from the direct use of our cosmogenic model ages they still correspond to a relatively high slip rate for the central ATF.

[35] Farther to the west, the age of the 2080 ± 100 m offset of EC relative to the eastern glacier, EG (Figure 11b), is 66.2 ± 1.8 ka, based upon the tight cluster of $^{10}$Be model ages. The resulting slip rate, which again must be taken as a maximum due to the potential effect of erosion, is 31.4 ± 1.7 mm/yr, in good agreement with the rate derived from the paleoconfluence edges. It is plausible that because of erosion, the model ages underestimate the true ages of these samples and that the EC samples could have been deposited just after the end of the last interglacial, at ~109 ka. The latter age would yield a lower slip rate estimate of ~20 mm/yr. The age of the 1400 ± 100 m offset of the M1 moraine relative to WG is constrained by a tight cluster of model ages at 47.1 ± 4.4 ka, yielding a rate of 29.7 ± 3.5 mm/yr. An erosion rate of 10 m/Myr would increase this age to ~65 ka and result in a lower bracket of ~21 mm/yr. Recall, however, that the lack of dispersion for the model ages obtained on both of these surfaces is consistent with a low erosion rate. The slip rates determined by propagating the individual ages and uncertainties for samples from M1, EC, and CP along with the associated offset data yield a weighted mean slip rate of 30.7 ± 0.9 mm/yr (Figure 19).

[36] Dating within the western valley is not as secure as in the eastern paleoconfluence, with ages displaying considerably more scatter (Figures 15 and 16). However, with the exception of a single 23.8 ka sample along the fault trace, and one 6.6 ka sample north of the fault, the absence of samples younger than 34 ka from the paleoconfluence suggests that neither EG nor WG occupied this area south of the fault after 34 ka (Figure 16). WG must have been flowing in the western valley after that time, probably starting at the beginning of the glacial maxima at the end of the MIS-3 interstadial (~35 ka, Figures 15, 16, and 17). The younger samples within WV confirm the inference that WG alone carved this valley beginning at 34 ± 4 ka (age and error inferred from Guliya $^{18}$O record). This age estimate is unlikely to be affected by erosion, since erosion has little effect on model ages in this age range (Figure 14). With this

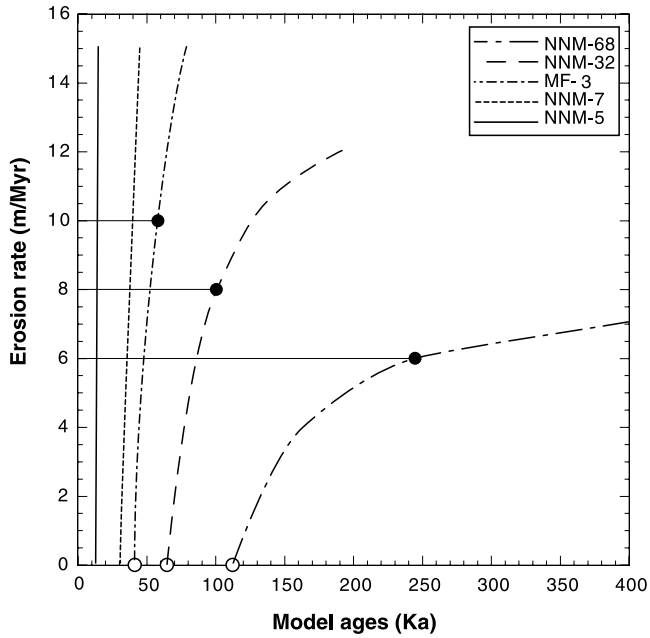


**Figure 14.** Effects of erosion on model ages of keys samples from the Sulamu Tagh (see text). The model uses the $^{10}$Be concentrations in selected samples and calculates an apparent age for different erosion rates. The solid circles represent model ages specifically discussed in the text.

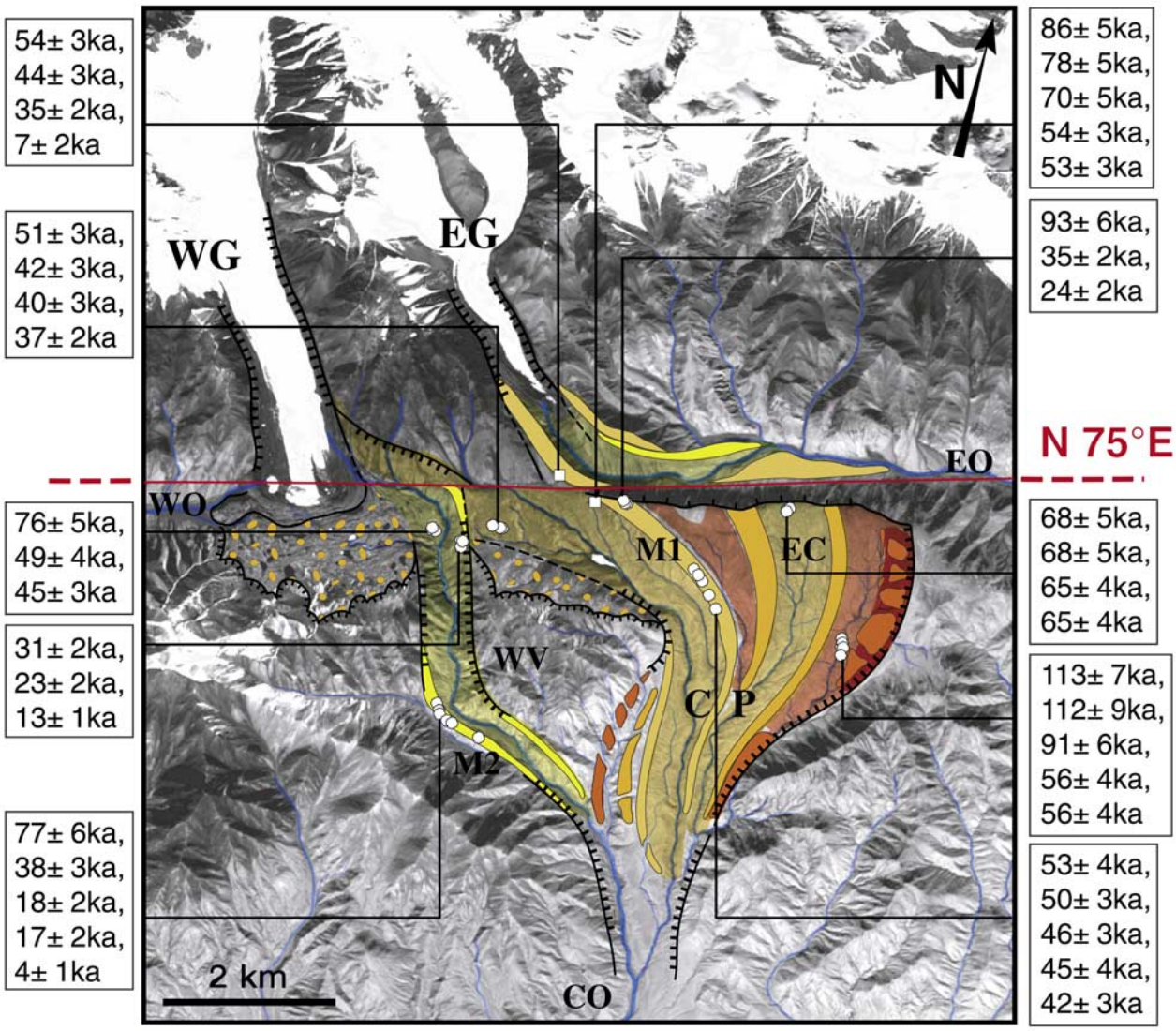


**Figure 15.** Field map of offset paleoglacial valleys on south slope of Sulamu Tagh (37.8°N, 87.4°E; 4450–4960 m asl), overlain on SPOT image KJ 222-274. Positions (open symbols) and $^{10}$Be model ages (boxes) of moraine samples are shown. The progression of colors from red to yellow represents increasingly younger paleoglacial valleys and lateral moraines. The dotted areas are young undifferentiated tills, on the till-covered bench. Bold lines with ticks mark outer limits of ice stream incision and south edge of till bench.

age, the offset of the eastern edge of WV relative to that of WG, 1020 ± 100 m, results in a slip rate of 30.0 ± 4.6 mm/yr. The incision of the postglacial streams S1 and S2 on the bench between WG and EG has not been dated directly. However, if this incision were coeval with post-LGM warming, then its inferred age might be that of T2 at Cherchen He, 16.6 ± 3.9 ka, resulting in rates of 30.1 ± 7.2 and 27.7 ± 6.6 mm/yr for the 500 ± 20 and 460 ± 20 m, respectively, stream offsets (Figure 20). The overall interpretation for the Sulamu Tagh that we propose may not be unique, but alternative scenarios matching local glacial features across the fault would yield faster slip rates. This would be the case if other, smaller glaciers west of WG were inferred to have flooded and shaped the paleoconfluence south of the fault or if the eastern channels of that confluence had been incised by advances of the western glacier.

[37] The slip rate defined by the offset of WV provides one argument against significant erosional effects on the model ages. As the <34 ka model ages cannot be significantly perturbed by erosion, the WV slip rate (30 ± 4.6 mm/yr) must be considered reasonably robust relative to those derived from the older markers. If indeed the lower slip rates, ~20 mm/yr, derived from "erosion-aged" older markers were correct, then a 50% increase in the long-term slip rate would have occurred. This seems implausible. Eastward propagation of the ATF could have resulted in increasing slip rates with time [*Meyer et al.*, 1998], but the eastern tip of the ATF was already more than 1000 km east of Sulamu Tagh in the Middle Pleistocene [*Métivier et al.*, 1998].

[38] It is worthwhile to consider the time necessary to produce the offsets observed at Sulamu Tagh if the long-term slip rate there had been on order of that modeled from

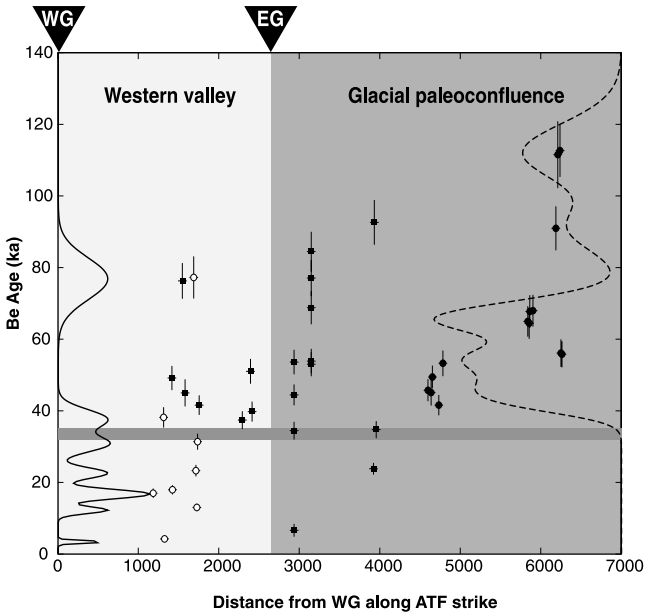


**Figure 16.** The $^{10}$Be model ages of Sulamu Tagh samples as a function of position, projected on a line trending N75°. Western valley samples (open circles), glacial paleoconfluence samples (solid circles), and samples near the fault zone in WV and CP (solid squares). Summed Gaussian density function (individual ages are represented as Gaussian distributions with a FWHM equal to the standard deviation); Western Valley samples are on left side and paleoconfluence samples on right side. The horizontal band brackets the age between the onset of cooling observed in the Guliya ice cap $^{18}$O record [*Thompson et al.*, 1997] and the boundary between MIS 2 and MIS 3, the time period in which the western glacier may have advanced into the Western Valley alone.

recent GPS observations at 90°E, 9 ± 4 mm/yr [*Bendick et al.*, 2000]. At this rate, the 3660 m offset would have taken ~400,000 years to accumulate. Both marine and continental stable isotope paleotemperature records display temperature minima at ~450, ~350, and ~250 ka. Had glacial maxima associated with either the ~450 or ~350 ka temperature minima been responsible for the initial excavation of the confluence, then we would expect to see some evidence of samples with ages older than 110 ka within the population of cosmogenic dates. Alternatively, glacial advances between ~450 and 110 ka might not have crossed the fault. However, this seems rather implausible, since even during the Holocene interglacial, WG did not fully withdraw north of the fault.

[39] The self-consistency of the rates obtained by matching cumulative offsets of very different sizes (166–3660 m), accrued during periods varying from 6 to 113 ka, constrained by three different dating techniques in two diverse geomorphic environments, is remarkable (Figure 20). The linearity of the offset and rate versus model age data (Figures 20 and 21) in itself constitutes a strong argument in favor of low erosion rates with negligible effect on the model ages. Over timescales of $10^5$ years, it is expected that, in general, large active strike-slip faults should slip at a constant rate. For instance, the slip rate on the Kunlun Fault has been shown to remain constant over the last 40,000 years [*Van der Woerd et al.*, 2000, 2002b]. Importantly, the slip rate obtained from the largest offset on the Kunlun Fault (~400 m) was constrained by radiocarbon dating that is not influenced by erosion and by pairing the age of an upper, fill terrace to the offset of a riser dug into it. If erosion had played a significant role, the offset versus model age trends at high erosion rates should depart from linearity (Figure 21). Rates obtained from larger, older offsets would be higher than the true value as the effect of erosion on model ages is greatest for older samples (Figures 14 and 21); the magnitude of the departure would decrease with offset.

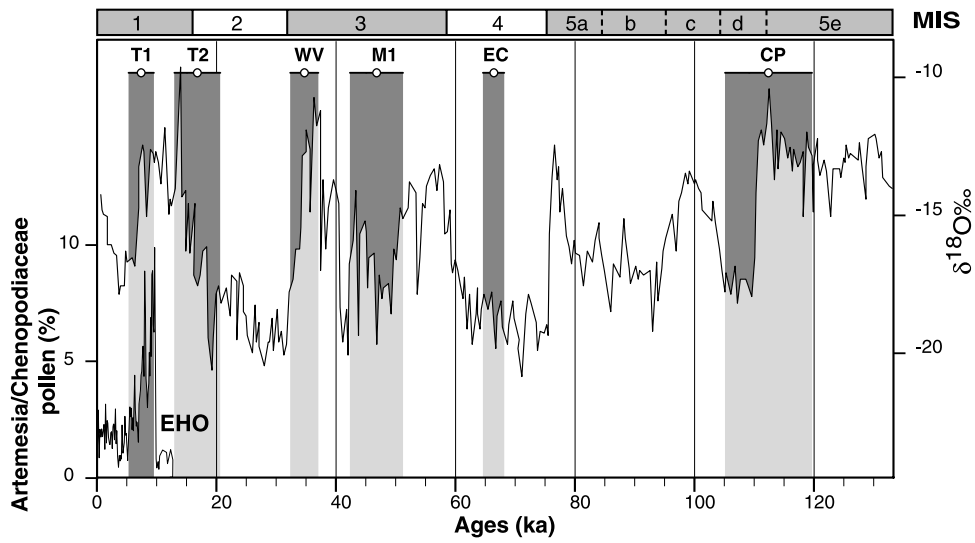


**Figure 17.** The $\delta^{18}$O changes in the core samples of Guliya ice cap (left axis) [*Thompson et al.*, 1997] and the regional moisture proxy ratio of Artemisia-Chenopodiacae pollen, from Sumxi Co sediment core (right axis) [*Gasse et al.*, 1991] compared to the dated features at Cherchen He and Sulamu Tagh. The upper *x* axis shows the SPECMAP marine isotope stages. EHO is the early Holocene Optimum.

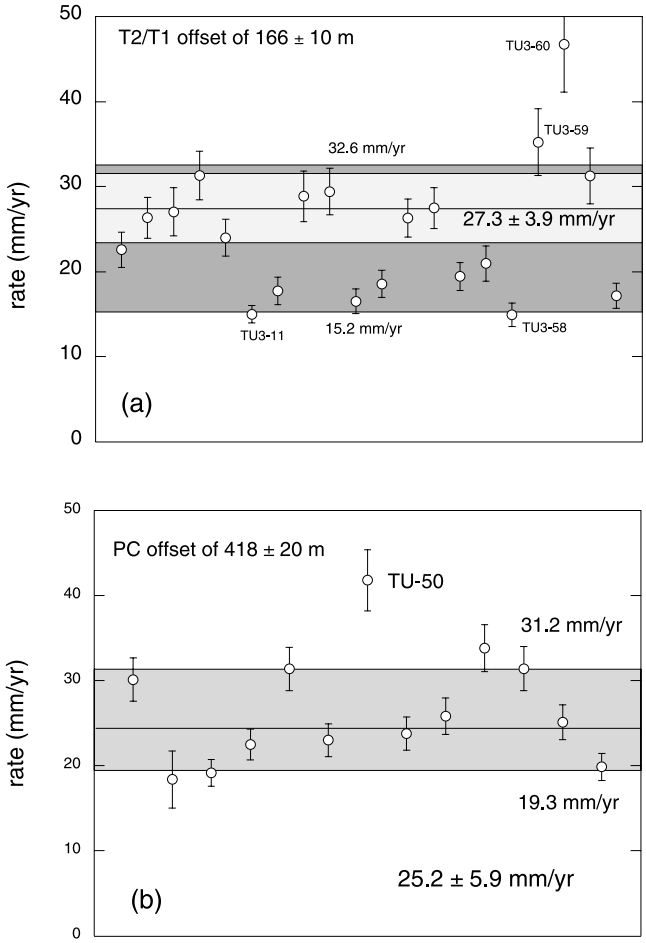


**Figure 18.** Slip rate determinations for Cherchen He. (a) T2/T1. The individual data points (○) represent the slip rate and 1σ error determined by propagation of the individual $^{10}$Be surface age and offset measurements (those not excluded using Chauvenet's criterion, see text) in conjunction with their 1σ errors. For comparison, the inner bracket (light gray) represents the range of slip rates (including 1σ errors) obtained from the radiocarbon date (6.4 ± 0.1 ka) on both the 160 ± 10 m and 180 ± 10 m offsets (27.0 ± 2.7 mm/yr). The outer bracket (medium gray) represents the range (15.8–32.1 mm/yr) obtained by propagating the average $^{10}$Be age and standard deviation (7.3 ± 2.2 ka) and both offset measurements; this bracket captures a majority of the individual slip rate measurements. (b) PC offset (418 ± 20 m). The large bracket, 19.3–31.2 mm/yr, is the range obtained by propagating the average age and standard deviation (16.6 ± 3.9 ka), 25.2 ± 5.9 mm/yr (Table 4) and again captures a majority of the individual determinations including 1σ errors.

Attempts to apply linear fits to offset versus "erosion influenced" model age data will result in higher slip rates and decreasing "goodness of fit" (as evidenced by increasing MSWD) as the erosion rate increases. For instance, assuming offset and age uncertainties similar to ours, a constant slip rate of 30 mm/yr yields a MSWD ~0. Erosion rates of 10 and 20 m/Myr yield offset versus model age fits with MSWD = 1.58 and 4.4, respectively, and linear fits yield nonzero intercepts (Figure 21). Linear regression of the 6 offset-model age pairs from the Sulamu Tagh yields a slip rate of 32.6 ± 2.8 mm/yr with MSWD = 0.04 (Figure 21). Regression of the combined Sulamu Tagh and Cherchen He offset versus model age data (9 pairs) yields a slip rate of 31.7 ± 1.9 mm/yr with MSWD = 0.14. The clear linearity of these trends is good argument against significant erosional effects on the model ages and supports the higher slip rates estimates presented above.

[40] Another estimate of the potential effects of erosion can be obtained by the comparing the rates at Cherchen He and Sulamu Tagh; the weighted mean slip rate estimates with standard errors are 26.3 ± 1.4 mm/yr (MSWD = 0.20) and 31.0 ± 1.7 mm/yr (MSWD = 0.13) at Cherchen He and Sulamu Tagh, respectively (Table 4). The lower rate at Cherchen He is consistent with minimum brackets obtained from the PC offset and the radiocarbon dating. Comparison of the cosmogenic and radiocarbon dates also suggests that this rate may be influenced by inheritance of predepositional cosmogenic nuclides. Similarly, Sulamu Tagh provides a good maximum bound due to the potential of erosion to reduce model ages. If we ignore the errors and assume that the 26.3 mm/yr rate at Cherchen He is the correct rate for the central ATF, then the higher rate obtained from the Sulamu Tagh data could be reconciled with the Cherchen He rate if the model ages at the Sulamu Tagh had been decreased due to a higher erosion rate. The erosion rate required to reconcile the slip rates at the different sites is only 2–3 m/Myr and represents an upper bound on the erosion rate. An erosion rate of this magnitude would not significantly perturb the linearity of the offset versus model age curves. Regression of offset versus model age data generated by the model presented in the previous paragraph and using an erosion rate of 2 m/Myr yields MSWD = 0.134, comparable to what we obtain at Sulamu Tagh and Cherchen He.

[41] The average rate obtained by propagating all of the offset-age pairs at Cherchen He and the rates at Sulamu Tagh, 41 determinations in all, is 26.9 ± 6.9 mm/yr (Figure 22a) and range from 14.9 to 46.7 mm/yr. This average rate is in excellent agreement with the rate obtained from the radiocarbon constraint on the T2/T1 offset at Cherchen He. The data are not normally distributed (MSWD = 9) and are skewed to lower values, as one would expect if the ages were perturbed by inheritance. An alternative estimate of the error associated with the rate is obtained from the 10% and 90% cumulative frequency interval around the median rate (Figure 22b), which yields a rate of $27.3^{+6.2}_{-9.7}$ mm/yr. The lower bracket, 17.6 mm/yr, is consistent with the lower bound, 18.4 mm/yr, obtained from the incision of PC into T2 at Cherchen He (Figure 22a). As the skewness in the data and resulting uneven error bars in our alternate estimate of uncertainty are likely due to the influence of inheritance for the cosmogenic nuclides, the simple average and standard deviation may better reflect the true uncertainty here. However, the difference between the two estimates is small.

[42] The millennial slip rate, 26.9 ± 6.9 mm/yr, integrated over ~110,000 years, near 87°E is compatible with those deduced from morphochronology on the eastern stretch of the fault near Aksay (~20 mm/yr at 94°E

**Table 4.** Offset, Age and Slip Rate Estimates for Cherchen He and Sulamu Tagh

| Feature | Offset (m) | Minimum Age,[a] ka | Maximum Rate,[b] mm/yr | Maximum Age Estimate,[c,d] ka | Minimum Bounding Rate,[c,d] ka |
|---|---|---|---|---|---|
| | | | *Cherchen He* | | |
| T2/T1, WS | 180 ± 10 | 6.4 ± 0.1 | 28.1 ± 3.2 | 10 ± 0.7[c] | 18.0 ± 2.4[c] |
| T2/T1, ES | 166 ± 10 | 6.4 ± 0.1 | 25.9 ± 1.6 | 10 ± 0.7[c] | 16.6 ± 1.53 |
| PC | 418 ± 20 | 16.6 ± 3.9[e] | 25.2 ± 5.9 | | |
| Weighted mean | | | 26.3 ± 1.4 (MSWD = 0.2) | | |
| | | | *Sulamu Tagh* | | |
| CP | 3660 ± 300 | 112.7 ± 7.3[f] | 32.5 ± 3.4 | 190 ± 10[d] | 19.3 ± 1.9[d] |
| EC | 2080 ± 100 | 66.2 ± 1.8[g] | 31.4 ± 1.7 | 109 ± 10[d] | 19.1 ± 2.1[d] |
| M1 | 1400 ± 100 | 47.1 ± 4.4[g] | 29.7 ± 3.5 | 65 ± 5[d] | 21.5 ± 2.3[d] |
| WV | 1020 ± 100 | 34 ± 4[h] | 30.0 ± 4.6 | | |
| S1 | 500 ± 20 | 16.6 ± 3.9[i] | 30.1 ± 7.2 | | |
| S2 | 460 ± 20 | 16.6 ± 3.9[i] | 27.7 ± 6.6 | | |
| Weighted mean | | | 31.0 ± 1.3[j] (MSWD = 0.14) | | |

[a]Errors on individual sample ages are obtained by propagating the standard deviation from the $^{10}$Be concentration distribution for a population of samples and the 6% uncertainty on production rate [*Stone*, 2000] and 3.3 and 2.8% uncertainties for decay constants of $^{10}$Be and $^{26}$Al, respectively [*Gosse and Phillips*, 2001].
[b]Errors on the slip rate are obtained by propagating the error on the offset and age in quadrature.
[c]Maximum age estimates at Cherchen He are obtained from the youngest cobble on the surface above an offset riser.
[d]Alternative age constraints at Sulamu Tagh are obtained by associating a dated feature with an earlier marine isotope stage (see text).
[e]Error is 1σ for the "accepted" population of surface samples (see Figure 13).
[f]Oldest sample from CP, NNM-68, with error as described in footnote a.
[g]Error is 1σ for the population of surface samples (see Figure 15).
[h]Age and error inferred from Guliya ice cap $^{18}$O record (see text).
[i]Age inferred from correlation with T2 surface at Cherchen He.
[j]Average and error of the mean includes CP, EC, M1, and model-dependent estimates from WV, S1, and S2.

[*Mériaux et al.*, 1997]) or on the Haiyuan Fault (19 ± 5 mm/yr at 102°E [*Lasserre et al.*, 1999]) and with shortening rates more crudely estimated across the Qaidam basin and Qilian Shan [*Meyer et al.*, 1998]. The decrease in slip rates toward the east probably involves transfer of slip to thrust faults, starting around 89°E. Some of these thrusts are large, north vergent and bound mountain ranges that rise up to 6000 m. This is the case for the Tanghenan Shan thrust, which has been demonstrated to have vertical throw rates of 5 ± 2 mm/yr near Subei [*Van der Woerd et al.*, 2001]. Farther east, the Yumen thrust, with opposite vergence and which does not dip under a high mountain range [*Meyer et al.*, 1998], has been interpreted to show much lower vertical throw rates, 0.3–0.4 mm/yr [*Hetzel et al.*, 2002]. Since that thrust is short, unconnected to other large regional faults, in particular the ATF, and not linked with the rise of one of the main ice-capped mountain ranges of NE Tibet, such a slow value is not particularly surprising. Furthermore, it is no surprise that an overall eastward decrease in strike-slip rate on the ATF and in the vertical throw rates on associated subperpendicular thrusts is observed. It is consistent with, and can be viewed as a direct consequence of, the northeastward growth of the Tibetan Plateau and of the northeastward propagation of the ATF [*Meyer et al.*, 1998]. What the low rate on the Yumen thrust may indicate is that this eastward decrease is even stronger, with a discrete step from millimeter per year to submillimeter per year rates, as one crosses the topographic step marked by the Qilian Shan frontal thrust, northern boundary of the Tibet-Qinghai plateau.

## 5. Conclusions

[43] Our morphochronological rate at 87°E differs markedly from the ~9 mm/yr slip rate derived from GPS measurements at 90°E [*Bendick et al.*, 2000], and from other more regional GPS slip rates [*Chen et al.*, 2000; *Shen et al.*, 2001]. Disparities in slip rates may result from some combination of measurement error, different observation intervals, along-strike variations, interseismic strain, and/or stress interactions between faults. Here the disparity is too large to be accounted for by variations in rate along strike. Relative to the long-term rate on the Haiyuan Fault, the 90°E GPS rate would imply east-west extension (~10 mm/yr) in the western Qilian Shan, a rate comparable

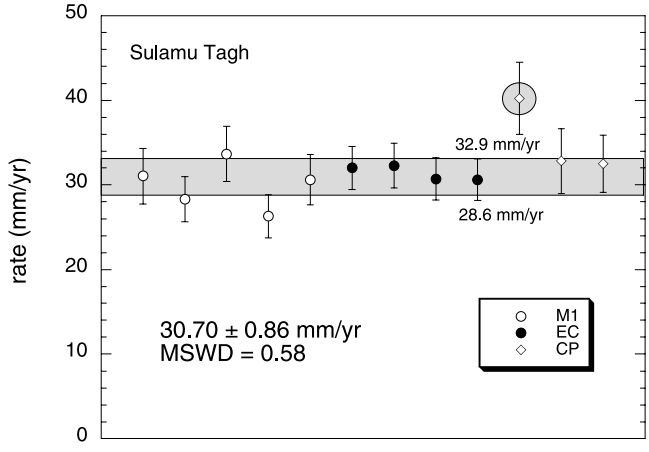


**Figure 19.** Propagation of individual Sulamu Tagh $^{10}$Be ages and offsets for M1, EC, and CP to obtain a distribution slip rates. The weighted mean and standard error for 11 measurements is 30.70 ± 0.86 mm/yr (the one rate near 40 mm/yr, shaded circle was not included). The shaded bracket (28.6–32.9 mm/yr; light gray) is the 1σ bracket around the average.

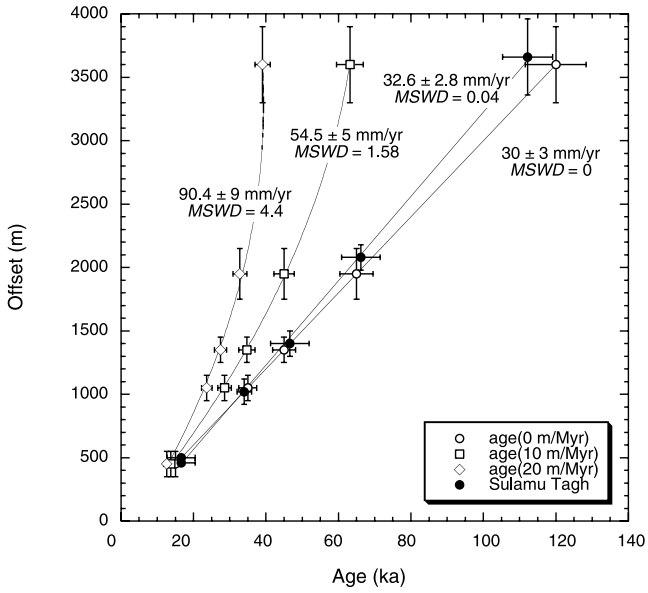


**Figure 20.** Effects of erosion rate on the apparent slip rate for a fault with a constant slip rate over time. For a fixed set of offset measurements, we assume a slip rate of 30 mm/yr with offsets, ages, and errors similar to those observed at Sulamu Tagh. For the 10 and 20 m/Myr models we assume that the age is the same as in the zero erosion rate model but recalculate the nuclide abundance for the different erosion rates. A ''zero erosion rate model age'' is then derived from these ''erosionally decreased'' nuclide concentrations, against which we plot the observed offsets. The effect of erosion in decreasing the model ages is most apparent for the oldest samples, and as erosion rate increases, the slip rate plots depart from linearity and the apparent slip rate increases dramatically. The 10 and 20 m/Myr are fit with parabolas to better display the nonlinearity; however, the rates and MSWDs are from linear regression. For comparison, we plot the six offset age pairs from the Sulamu Tagh (Table 4).

to current extension in the Red Sea. Similarly, relative to the Cherchen-Sulamu Tagh rate, the 90°E GPS rate would require the presence of a Himalayan size range along the Qiman Tagh (∼20 mm/yr convergence). Neither is observed. Since the difference in observation interval is large, it seems preferable to explain the disparity between GPS and morphochronologic rates as due to transient interseismic strain or clustering of earthquakes. There is clear suggestion of transient strain in the 90°E GPS results [*Bendick et al.*, 2000], because stations near the fault show larger relative displacements than stations farther from it. In any case, assessing thoroughly this disparity will have to await denser instrumentation since, with the exception of the deployment of *Bendick et al.* [2000], there are only three GPS monuments within a 500 km radius of the Cherchen He and Sulamu Tagh [*Wang et al.*, 2003]. That we obtain the same rate for intervals between ∼6000 and 16,000 years, however, suggests that transients cannot persist beyond 6000 years. The fact that slip rates on the Kunlun Fault remain constant at various sites over intervals ranging from 1800 to 37,000 years [*Van der Woerd et al.*, 2000] suggests even shorter transients.

[44] Although the current worldwide data set is small, disparities between decadal and millennial slip rates are observed elsewhere. For instance, the millennial slip rate on the Kunlun Fault is ∼12 mm/yr [*Van der Woerd et al.*, 2000] while the rate first determined by GPS was ∼6mm/yr [*Chen et al.*, 2000]. Similarly, an InSAR-derived surface strain map of the Eastern Mojave region over 8 years cannot resolve lateral slip on the Garlock Fault [*Peltzer et al.*, 2001], while the long-term rate determined by radiocarbon dating of offset lacustrine shorelines along this fault is ∼7 mm/yr [*McGill and Sieh*, 1991]. Alternatively, the decadal rate on the conjugate Blackwater Fault is faster than the estimated millennial rate [*Peltzer et al.*, 2001]. This is also the case for the Owens Valley Fault [*Lee et al.*, 2001].

[45] Such disparities indicate that far-field, short-term measurements need not yield the near-field, long-term slip rate in continental settings. This suggests that the slip rates on faults may vary over timescales of 100–1000 years as a response to episodic strain accumulation that in turn may lead to seismic clustering [*Peltzer et al.*, 2001; *Rockwell et al.*, 2000]. Mechanical interaction between conjugate faults has been suggested as the source of the decadal-millennial velocity disparity and oscillatory seismic moment release observed for the Garlock-Blackwater system [*Peltzer et al.*, 2001]. Similarly, oscillatory seismic release on the North and East Anatolian faults in Turkey [*Ambraseys*, 1973] has been modeled as the result of mechanical interactions between conjugate faults [*Hubert-Ferrari et al.*, 2003]. While comparable seismic evidence is lacking for the Altyn Tagh and Karakorum Faults, they form a large-scale set of conjugate faults similar to the North and East Anatolian faults. It should also be noted that the Kunlun

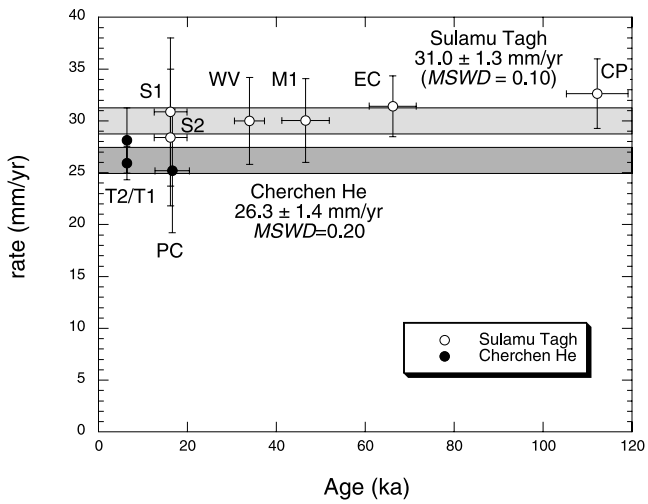


**Figure 21.** Summary of slip rate measurements from Cherchen He and Sulamu Tagh on the central Altyn Tagh Fault during the last glacial cycle (Table 4). Open symbols are the preferred slip rate estimates for Sulamu Tagh. The weighted mean for the six determinations is 31.0 ± 1.7 mm/yr; the shaded region (light gray) indicates the 1σ bracket on the mean rate. The bracket obtained from the weighted mean of the three Cherchen He determinations, 26.3 ± 1.4 mm/yr, is shown by the lower shaded region (medium gray).

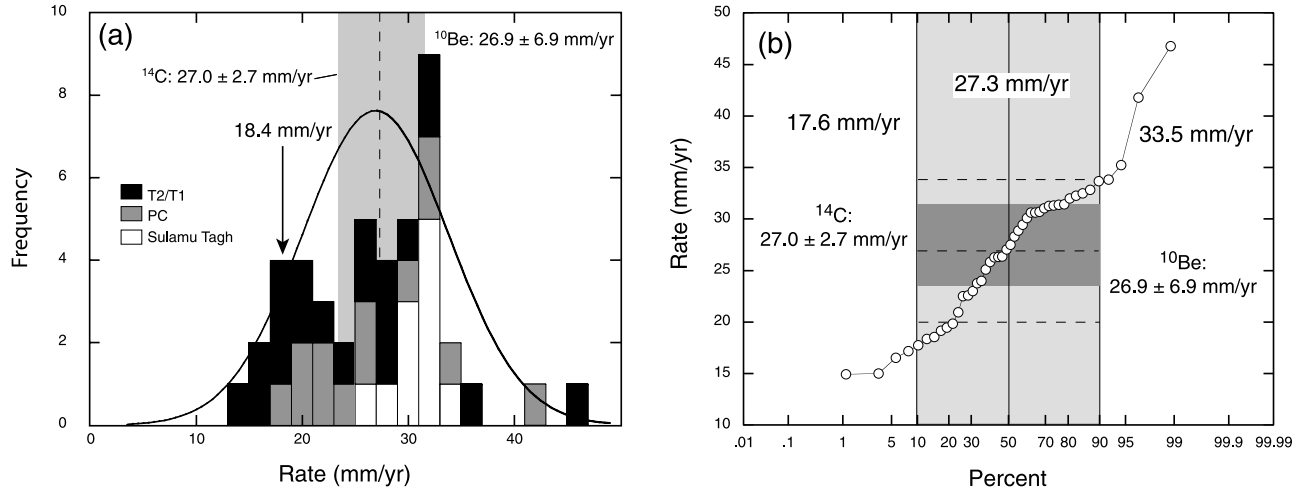


**Figure 22.** (a) Histogram of rates determinations from the Cherchen He and Sulamu Tagh. The average rate and standard deviation is 26.9 ± 6.9 mm/yr. The Gaussian distribution for this average as standard deviation is given by the solid line. The minimum rate obtained from the offset of PC at Cherchen He, 18.4 mm/yr is shown for reference. The shaded region in the center of the diagram shows the age and uncertainty associated with the radiocarbon age constraints on the T2/T1 offset at Cherchen He. (b) Cumulative histogram of rates from the Cherchen He and Sulamu Tagh. The median rate is 27.3 mm/yr. The light gray shaded region shows the range of rates between 10% and 90% cumulative frequency. The horizontal dashed lines give the error bracket determined from the $^{10}$Be dating. The darker gray band shows the age and uncertainty associated with the radiocarbon age constraints on the T2/T1 offset at Cherchen He.

Fault, which is subparallel to the Altyn Tagh, has experienced three $M_w > 7.5$ earthquakes in the last 70 years, two in the last decade [*Peltzer et al.*, 1999; *Van der Woerd et al.*, 2002a], while average recurrence times of 400–900 years are suggested by the long-term slip rate and characteristic slip measurements [*Van der Woerd et al.*, 1998, 2000, 2002b]. Such episodic moment release on the Kunlun Fault, along with the correlative decadal-millennial slip rate disparity it implies, may reflect mechanical interactions between the various faults that cross the Tibetan Plateau.

[46] At the other extreme, a number of total offset markers along the ATF have now been defined and the inferred long-term geological slip rates can be compared with our data. These comparisons are not straightforward, however, as the inferred geologic slip rate and total offset are intimately related to the long-term evolution and growth of the ATF and may vary along strike. If the fault initiated in the western Kunlun and propagated eastward, then both the slip rate and the offset recorded by pre-Tertiary piercing points should both decrease to the east [*Meyer et al.*, 1998; *Tapponnier et al.*, 2001]. The majority of the pre-Tertiary piercing points are found along the central and eastern portions of the fault and yield offsets ranging from 260 to 500 km [*Gehrels et al.*, 2003; *Ritts and Biffi*, 2000; *Sobel et al.*, 2001; *Yang et al.*, 2001; *Yin et al.*, 2002; *Yue et al.*, 2001].

[47] West of Mangnai (M, Figure 1), *Yue et al.* [2001] tentatively reconstructed the offsets of the Xorkol basin (91°–92°E) north of the ATF and of its inferred Oligocene–post-early Miocene source regions to the south, obtaining values of ~380 km and 300 km, respectively, corresponding to a long-term slip rate of 12–16 mm/yr, in agreement with the late Pleistocene-Holocene rate we find at Aksay (A, Figure 1) [*Mériaux*, 2002]. Similarly, dating of detrital zircons from Miocene conglomerates in the Xorkol basin and their presumed source rocks in the Qilian Shan and northern Qaidam regions south of the fault yields a rate of ~10 mm/yr (165 km/16.4 Ma) [*Yue et al.*, 2004]. In contrast, linking sedimentation patterns based on detailed oil company well logs in the Qaidam and Hexi Corridor to the eastward propagation of the ATF, *Métivier et al.* [1998] concluded that the eastern terminus of the ATF did not reach the longitude of the eastern Qaidam Basin until ~10 Ma. Uplift along the ATF and active thrusting in the Qilian Shan then closed the Qaidam to sediment discharge, producing a sharp increase in sedimentation rate within this Basin in the lower Pliocene. A much younger age may thus be associated with Yue et al.'s offsets, implying that the 10–16 mm/yr geological rate they propose is in fact a minimum. In this connection, paleomagnetic constraints from the sites along the ATF, Qaidam and Tarim basins indicate that 500 ± 130 km of displacement has accumulated along the ATF since 24 Ma, yielding a rate of ~20 mm/yr [*Chen et al.*, 2002].

[48] Near the western termination of the fault, *Peltzer and Tapponnier* [1988] noted that Late Permian–Early Triassic plutons in the western Kunlun [*Matte et al.*, 1996] were offset by >500 km across the ATF from coeval plutons in the eastern Kunlun. A recent reevaluation of this offset yields a similar estimate of the total offset, 475 ± 75 km [*Cowgill et al.*, 2003]. On the basis of the history of sedimentation for the southwestern Tarim Basin, Qaidam Basin and Hexi corridor, *Yin et al.* [2002] inferred that thrusting in the western Kunlun and along the Qiman Tagh and Northern Qaidam thrust systems began prior to 46 Ma and ~49 Ma, respectively and, by linking these thrusts to

the ATF, concluded that it must have been active since ~49 Ma. This, combined with the 475 ± 75 km total offset, yields a long-term slip rate of ~9 mm/yr. However, their temporal constraints are controversial. Where studied and dated in detail, rotations linked to slip on the ATF and shortening or uplift on thrusts adjacent to it are not of Eocene age. Near Subei for instance, magnetostratigraphic and structural data constrain rotation and folding to postdate ~20 Ma, and much of the fast shortening across thrusts connected to the ATF may be younger than 6 Ma [*Gilder et al.*, 2001; *Van der Woerd et al.*, 2001].

[49] On a greater scale, both Ar/Ar and apatite thermochronology in the Western Kunlun range [*Arnaud et al.*, 1991; *Sobel et al.*, 2001; *Sobel and Dumitru*, 1997; *Wang et al.*, 2003] and sediment accumulation rates in the Yecheng-Kashgar basin [*Métivier and Gaudemer*, 1997; *Métivier et al.*, 1999] indicate that even in the west, tectonic uplift and deformation related to transpression along the north edge of Tibet, hence along the ATF, did not start prior to ~20 Ma, at the beginning of the Miocene. Recent paleomagnetic results from Tertiary beds sampled chiefly in the western Qaidam and along the central Altyn Tagh [*Chen et al.*, 2002], also confirm that significant tectonic rotation related to strike-slip faulting began after the end of the Oligocene. More specifically, the latter authors suggest that much of the slip along the stretch of the ATF that bounds the Qaidam basin occurred between 24 and 10 Ma.

[50] Finally, on an even grander scale, a proposed initiation of slip on the ATF at ~50 Ma would predate by 13–22 Ma that initiation of slip on the Red River Shear Zone, ~36 Ma [*Gilley et al.*, 2003; *Leloup et al.*, 1995], and on the Gangdese Thrust system, ~27 Ma [*Yin et al.*, 1994]. which lie much closer to the Indo-Asian boundary, implying an improbable "out-of-sequence" onset of deformation, contrary to the more mechanically plausible evolution implied by other observations and approaches [*Lacassin et al.*, 1997; *Peltzer and Tapponnier*, 1988; *Replumaz and Tapponnier*, 2003]. Clearly, given the ongoing controversy on the ages and the problems raised by a ~50 Ma slip onset, the geological slip rate of ~9 mm/yr inferred by *Yin et al.* [2002] should only be regarded as a lower bound.

[51] In any event, pending more accurate results from further study of recent Quaternary deformation, our results imply that the present amount of shortening absorbed by the ATF system at 87°E, in a direction roughly perpendicular to the Himalayas, may be about 15 mm/yr, close to that on the Main Frontal Thrust in Nepal [*Bilham et al.*, 1997; *Lave and Avouac*, 2000]. Despite markedly different tectonic styles, the two rims of the Tibetan Plateau might then take up comparable fractions of India's convergence relative to Siberia [*Armijo et al.*, 1989; *Avouac and Tapponnier*, 1993; *Peltzer and Saucier*, 1996; *Peltzer and Tapponnier*, 1988]. The fast millennial slip rate we find on the central ATF, as well as recent results of similar studies [*Lasserre et al.*, 1999; *Van der Woerd et al.*, 2000], suggests that the large strike-slip faults of northern Tibet move at plate boundary velocities. Together with evidence for a trans-lithospheric low *P* wave velocity anomaly beneath the ATF [*Wittlinger et al.*, 1998], such high rates suggest that the mechanical behavior of the continental lithosphere may be dominated by strain localization. Hence block models and models including fault propagation probably provide a more adequate description of Asian lithospheric deformation [*Peltzer and Tapponnier*, 1988; *Tapponnier et al.*, 2001], and of continental deformation in other collision zones [*McClusky et al.*, 2000], than models assuming widespread, diffuse crustal strain driven by distributed viscous flow of the subcrustal upper mantle [*England and Houseman*, 1986; *England and Molnar*, 1997a, 1997b; *Holt*, 2000; *Holt et al.*, 2000].

[52] **Acknowledgments.** This work was performed under the auspices of the U.S. Department of Energy by University of California Lawrence Livermore National Laboratory under contract W-7405-Eng-48 under the sponsorship of the LDRD program. We benefited from 4 years of financial and logistical support from Institut National des Sciences de l'Univers, Centre National de la Recherche Scientifique (Paris, France) through programs IDYL and IT, and from the China seismological Bureau and the Ministry of Lands and Resources (Beijing, China). We thank B. Ralph for his assistance in scanning Corona images. We appreciate critical reviews by Bradley Ritts and an anonymous reviewer along with comments from Bob Anderson, J.-P. Avouac, Roger Bilham, and Grant Raisbeck on earlier versions of this work. This is IPGP contribution 1977 and University of California UCRL-JRNL-200220.

## References

Ambraseys, N. N. (1973), Value of historical record of earthquakes, *Nature*, *232*, 375–379.

Anderson, R. S., J. L. Repka, and G. S. Dick (1996), Explicit treatment of inheritance in dating depositional surfaces using in situ $^{10}$Be and $^{26}$Al, *Geology*, *24*(1), 47–51.

Armijo, R., P. Tapponnier, and H. Tonglin (1989), Late Cenozoic right-lateral strike-slip faulting in southern Tibet, *J. Geophys. Res.*, *94*(B3), 2787–2838.

Arnaud, N., R. Xu, and Y. Zhang (1991), Nouvelles données thermochronologiques sur le batholite du Kunlun et l'histoire thermique du nord du plateau Tibétain, *C.R. Acad. Sci.*, *312*(8), 905–911.

Avouac, J. P., and P. Tapponnier (1992), Kinematic model of active deformation in central-Asia, *C. R. Acad. Sci.*, *Ser. Ii*, *315*(13), 1791–1798.

Avouac, J. P., and P. Tapponnier (1993), Kinematic model of active deformation in central-Asia, *Geophys. Res. Lett.*, *20*(10), 895–898.

Bendick, R., R. Bilham, J. Freymueller, K. Larson, and G. H. Yin (2000), Geodetic evidence for a low slip rate in the Altyn Tagh fault system, *Nature*, *404*(6773), 69–72.

Bevington, P. R., and D. K. Robinson (2002), *Data Reduction and Error Analysis for the Physical Sciences*, 336 pp., McGraw-Hill, New York.

Bierman, P. R., and M. W. Caffee (2001), Slow rates of rock surface erosion and sediment production across the Namib Desert and escarpment, southern Africa, *Am. J. Sci.*, *301*, 326–358.

Bilham, R., et al. (1997), GPS measurements of present-day convergence across the Nepal Himalaya, *Nature*, *386*(6620), 61–64.

Bull, W. B. (1991), *Geomorphic Responses to Climatic Change*, 326 pp., Oxford Univ. Press, New York.

Chen, Y., S. Gilder, N. Halim, J. P. Cogné, and V. Courtillot (2002), New paleomagnetic constraints on central Asian kinematics: Displacement along the Altyn Tagh fault and rotation of the Qaidam Basin, *Tectonics*, *21*(5), 1042, doi:10.1029/2001TC901030.

Chen, Z., B. C. Burchfiel, Y. Liu, R. W. King, L. H. Royden, W. Tang, E. Wang, J. Zhao, and X. Zhang (2000), Global Positioning System measurements from eastern Tibet and their implications for India/Eurasia intercontinental deformation, *J. Geophys. Res.-Solid Earth*, *105*(B7), 16,215–16,227.

Clark, D. H., P. R. Bierman, and P. Larsen (1995), Improving in situ cosmogenic chronometers, *Quat. Res.*, *44*, 367–377.

Cowgill, E., A. Yin, T. M. Harrison, and W. Xiao-Feng (2003), Reconstruction of the Altyn Tagh fault based on U-Pb geochronology: Role of back thrusts, mantle sutures, and heterogeneous crustal strength in forming the Tibetan Plateau, *J. Geophys. Res.*, *108*(B7), 2346, doi:10.1029/2002JB002080.

England, P., and G. Houseman (1986), Finite strain calculations of continental deformation: 2. Comparison with the India-Asia collision zone, *J. Geophys. Res.*, *91*(B3), 3664–3676.

England, P., and P. Molnar (1997a), Active deformation of Asia: From kinematics to dynamics, *Science*, *278*, 647–650.

England, P., and P. Molnar (1997b), The field of crustal velocity in Asia calculated from Quaternary rates of slip on faults, *Geophys. J. Int.*, *130*, 551–582.

Gasse, F., et al. (1991), A 13,000–year climate record from western Tibet, *Nature*, *353*(6346), 742–745.

Ge, S., G. Shen, R. Wei, G. Ding, and Y. Wang (1992), *Active Altun Fault Zone Monograph*, 319 pp., State Seismol. Bur. of China, Beijing.

Gehrels, G. E., A. Yin, and X. F. Wang (2003), Detrital-zircon geochronology of the northeastern Tibetan plateau, *Geol. Soc. Am. Bull.*, *115*(7), 881–896.

Gilder, S., Y. Chen, and S. Sen (2001), Oligo-Miocene stratigraphy and rock magnetism of the Xishuigou section, Subei (Gansu Province, western China), *J. Geophys. Res.*, *106*(B12), 30,505–30,521.

Gilley, L. D., T. M. Harrison, P. H. Leloup, F. J. Ryerson, O. M. Lovera, and J.-H. Wang (2003), Direct dating of left-lateral deformation along the Red River shear zone, China and Vietnam, *J. Geophys. Res.*, *108*(B2), 2127, doi:10.1029/2001JB001726.

Gosse, J. C., and F. M. Phillips (2001), Terrestrial in situ cosmogenic nuclides: Theory and application, *Quat. Sci. Rev.*, *20*(14), 1475–1560.

Hancock, G. S., R. S. Anderson, O. A. Chadwick, and R. C. Finkel (1999), Dating fluvial terraces with Be-10 and Al-26 profiles: Application to the Wind River, *Wyoming*, *Geomorphology*, *27*(1–2), 41–60.

Herquel, G., P. Tapponnier, G. Wittlinger, J. Mei, and S. Danian (1999), Teleseismic shear wave splitting and lithospheric beneath and across the Altyn Tagh fault, *Geophys. Res. Lett.*, *26*(21), 3225–3228.

Hetzel, R., S. Niedermann, M. Tao, P. W. Kubik, S. Ivy-Ochs, B. Gao, and M. R. Strecker (2002), Low slip rates and long-term preservation of geomorphic features in central Asia, *Nature*, *417*(6887), 428–432.

Holt, W. E. (2000), Correlated crust and mantle strain fields in Tibet, *Geology*, *28*(1), 67–70.

Holt, W. E., N. Chamot-Rooke, X. Le Pichon, A. J. Haines, B. Shen-Tu, and J. Ren (2000), Velocity field in Asia inferred from Quaternary fault slip rates and global positioning system observations, *J. Geophys. Res.*, *105*(B8), 19,185–19,209.

Hubert-Ferrari, A., G. King, I. Manighetti, R. Armijo, B. Meyer, and P. Tapponnier (2003), Long-term elasticity in the continental lithosphere; modelling the Aden Ridge propagation and the Anatolian extrusion process, *Geophys. J. Int.*, *153*, 111–132.

Imbrie, J., J. D. Hays, D. G. Martinson, A. Mclntyre, A. C. Mix, J. J. Morley, N. G. Pisias, W. L. Prell, and N. J. Shackleton (1984), The orbital theory of Pleistocene climate: Support from a revised chronology of the marine delta $^{18}O$ record, in *Milankovitch and Climate, Part I*, edited by A. Berger et al., pp. 269–305, D. Reidel, Norwell, Mass.

Kohl, C. P., and K. Nishiizumi (1992), Chemical isolation of quartz for measurement of in situ-produced cosmogenic nuclides, *Geochim. Cosmochim. Acta*, *56*(9), 3583–3587.

Lacassin, R., H. Maluski, P. H. Leloup, P. Tapponnier, C. Hinthong, K. Siribhakdi, S. Chuaviroj, and A. Charoenravat (1997), Tertiary diachronic extrusion and deformation of western Indochina: Structural and $^{40}Ar/^{39}Ar$ evidence from NW Thailand, *J. Geophys. Res.*, *102*(B5), 10,013–10,037.

Lal, D. (1991), Cosmic ray labeling of erosion surfaces: In situ production rates and erosion models, *Earth Planet. Sci. Lett.*, *104*, 424–439.

Lasserre, C., et al. (1999), Postglacial left slip rate and past occurrence of $M \geq 8$ earthquakes on the western Haiyuan fault, Gansu, China, *J. Geophys. Res.*, *104*(B8), 17,633–17,651.

Lave, J., and J. P. Avouac (2000), Active folding of fluvial terraces across the Siwaliks Hills, Himalayas of central Nepal, *J. Geophys. Res.*, *105*(B3), 5735–5770.

Lee, J., J. Spencer, and L. Owen (2001), Holocene slip rates along the Owens Valley Fault, California: Implications for the recent evolution of the Eastern California Shear Zone, *Geology*, *29*(9), 819–822.

Leloup, P. H., R. Lacassin, P. Tapponnier, U. Scharer, D. L. Zhong, X. H. Liu, L. S. Zhang, S. C. Ji, and P. T. Trinh (1995), The Ailao Shan-Red River shear zone (Yunnan China), Tertiary transform boundary of Indochina, *Tectonophysics*, *251*(1–4), 3–84.

Matte, P., P. Tapponnier, N. Arnaud, L. Bourjot, J. P. Avouac, P. Vidal, L. Qing, Y. S. Pan, and W. Yi (1996), Tectonics of western Tibet, between the Tarim and the Indus, *Earth Planet. Sci. Lett.*, *142*(3–4), 311–330.

McClusky, S., et al. (2000), Global positioning system constraints on plate kinematics and dynamics in the eastern Mediterranean and Caucasus, *J. Geophys. Res.*, *105*(B3), 5695–5719.

McGill, S. F., and K. Sieh (1991), Surficial offsets on the central and eastern Garlock Fault associated with prehistoric earthquakes, *J. Geophys. Res.*, *96*(B13), 21,597–21,621.

Mériaux, A.-S. (2002), Détermination par datation cosmogénique des variations de la vitesse de glissement sur la faille de l'Atlyn Tagh depuis 100 ka, Ph.D. thesis, Univ. Paris VII, Paris.

Mériaux, A., P. Tapponnier, F. J. Ryerson, J. Van der Woerd, G. King, B. Meyer, R. Finkel, and M. Caffee (1997), Application of cosmogenic $^{10}Be$ and $^{26}Al$ dating to neotectonics of the Altyn Tagh Fault in central Asia (Gansu China), *Eos Trans. AGU*, *78*(46), Fall Meet. Suppl., F173.

Métivier, F., and Y. Gaudemer (1997), Mass transfer between the eastern Tien Shan and adjacent basins: Constraints on regional tectonics and topography, *Geophys. J. Int.*, *128*, 1–17.

Métivier, F., Y. Gaudemer, P. Tapponnier, and B. Meyer (1998), Northeastward growth of the Tibet plateau deduced from balanced reconstruction of two depositional areas: The Qaidam and Hexi Corridor basins, China, *Tectonics*, *17*(6), 823–842.

Métivier, F., Y. Gaudemer, P. Tapponnier, and M. Klein (1999), Mass accumulation rates in Asia during the Cenozoic, *Geophys. J. Int.*, *137*, 280–318.

Meyer, B., P. Tapponnier, L. Bourjot, F. Métivier, Y. Gaudemer, G. Peltzer, G. Shunmin, and C. Zhitai (1998), Crustal thickening in Gansu-Qinghai, lithospheric mantle subduction, and oblique, strike-slip controlled growth of the Tibet Plateau, *Geophys. J. Int.*, *135*, 1–47.

Molnar, P., et al. (1994), Quaternary climate-change and the formation of river terraces across growing anticlines on the north flank of the Tien-Shan, China, *J. Geol.*, *102*(5), 583–602.

Nishiizumi, K., E. L. Winterer, C. P. Kohl, J. Klein, R. Middleton, D. Lal, and J. R. Arnold (1989), Cosmic ray production rates of $^{10}Be$ and $^{26}Al$ in quartz from glacially polished rocks, *J. Geophys. Res.*, *94*(B12), 17,907–17,915.

Nishiizumi, K., C. P. Kohl, J. R. Arnold, J. Klein, D. Fink, and R. Middleton (1991), Cosmic ray produced $^{10}Be$ and $^{26}Al$ in Antarctic rocks: Exposure and erosion history, *Earth Planet. Sci. Lett.*, *104*, 440–454.

Owen, L. A., R. C. Finkel, M. W. Caffee, and L. Gualtieri (2002), Timing of multiple late Quaternary glaciations in the Hunza Valley, Karakoram Mountains, northern Pakistan: Defined by cosmogenic radionuclide dating of moraines, *Geol. Soc. Am. Bull.*, *114*, 593–604.

Peltzer, G., and F. Saucier (1996), Present-day kinematics of Asia derived from geologic fault rates, *J. Geophys. Res.*, *101*(B12), 27,943–27,956.

Peltzer, G., and P. Tapponnier (1988), Formation and evolution of strike-slip faults, rifts, and basins during the India-Asia collision: An experimental approach, *J. Geophys. Res.*, *93*(B12), 15,085–15,117.

Peltzer, G., P. Tapponnier, and R. Armijo (1989), Magnitude of Late Quaternary left-lateral displacements along the north edge of Tibet, *Science*, *246*, 1285–1289.

Peltzer, G., F. Crampe, and G. King (1999), Evidence of nonlinear elasticity of the crust from the Mw 7. 6 Manyi (Tibet) earthquake, *Science*, *286*, 272–276.

Peltzer, G., F. Crampe, S. Hensley, and P. Rosen (2001), Transient strain accumulation and fault interaction in the Eastern California Shear Zone, *Geology*, *29*(11), 975–978.

Poisson, B. (2002), Impact du climat et de la tectonique sur l'évolution géomorphologique d'un piémont, Exemple du piémont Nord Tian Shan depuis la fin du Pléistocène, Ph.D. thesis, Univ. Paris XI, Paris.

Poisson, B., and J.-P. Avouac (2004), Holocene hydrological changes inferred from alluvial stream entrenchment in North Tian Shan (northwestern China), *J. Geol.*, *112*(2), 231–249.

Replumaz, A., and P. Tapponnier (2003), Reconstruction of the deformed collision zone between India and Asia by backward motion of lithospheric blocks, *J. Geophys. Res.*, *108*(B6), 2285, doi:10.1029/2001JB000661.

Ritts, B. D., and U. Biffi (2000), Magnitude of post-Middle Jurassic (Bajocian) displacement on the Altyn Tagh Fault, northwest China, *Geol. Soc. Am. Bull.*, *112*, 61–74.

Rockwell, T. K., S. Lindvall, M. Herzberg, D. Murbach, T. Dawson, and G. Berger (2000), Paleoseismology of the Johnson Valley, Kickapoo, and Homestead Valley faults; clustering of earthquakes in the Eastern California Shear Zone, *Bull. Seismol. Soc. Am.*, *90*, 1200–1236.

Ryerson, F. J., G. Peltzer, P. Tapponnier, R. C. Finkel, A.-S. Meriaux, and J. Van der Woerd (1999), Active slip-rates on the Altyn Tagh Fault–Karakax Valley segment: Constraints from surface exposure dating, *Eos Trans. AGU*, *80*(46), Fall Meet. Suppl., F1008–F1009.

Shen, F., L. H. Royden, and B. C. Burchfiel (2001), Large-scale crustal deformation of the Tibetan Plateau, *J. Geophys. Res.*, *106*(B4), 6793–6816.

Sieh, K. E., and R. H. Jahns (1984), Holocene activity of the San-Andreas Fault at Wallace-Creek, California, *Geol. Soc. Am. Bull.*, *95*, 883–896.

Small, E. E., R. S. Anderson, J. L. Repka, and R. Finkel (1997), Erosion rates of alpine bedrock summit surfaces deduced from in situ $^{10}Be$ and $^{26}Al$, *Earth Planet. Sci. Lett.*, *150*, 413–425.

Sobel, E. R., and T. A. Dumitru (1997), Thrusting and exhumation around the margins of the western Tarim basin during the India-Asia collision, *J. Geophys. Res.*, *102*(B3), 5043–5063.

Sobel, E. R., N. Arnaud, M. Jolivet, B. D. Ritts, and M. Brunel (2001), Jurassic to Cenozoic exhumation of the Altyn Tagh range, northwest China, constrained by $^{40}Ar/^{39}Ar$ and apatite fission track thermochronology, in *Paleozoic and Mesozoic Tectonic Evolution of Central Asia:From Continental Assembly to Intracontinental Deformation*, edited by M. S. Hendrix and G. A. Davis, *Mem. Geol. Soc. Am.*, *194*, 247–267.

Stone, J. O. (2000), Air pressure and cosmogenic isotope production, *J. Geophys. Res.*, *105*(B10), 23,753–23,759.

Stuiver, M., P. J. Reimer, E. Bard, J. W. Beck, G. S. Burr, K. A. Hughen, B. Kromer, G. McCormac, and M. Spurk (1998), INTCAL98 radiocarbon age calibration, 24000–0 cal BP, *Radiocarbon*, *40*, 1041–1084.

Tapponnier, P., X. Zhiqin, B. Meyer, F. Roger, N. Arnaud, G. Wittlinger, and Y. Jingsui (2001), Asymmetric, stepwise rise and growth of the Tibet Plateau, *Science*, *294*, 1671–1677.

Thompson, L. G., T. Yao, M. E. Davis, K. A. Henderson, E. Mosley-Thompson, P. N. Lin, J. Beer, H. A. Synal, J. ColeDai, and J. F. Bolzan (1997), Tropical climate instability: The last glacial cycle from a Qinghai-Tibetan ice core, *Science*, *276*, 1821–1825.

Van der Woerd, J. W., F. J. Ryerson, P. Tapponnier, Y. Gaudemer, R. Finkel, A. S. Meriaux, M. Caffee, G. G. Zhao, and Q. L. He (1998), Holocene left-slip rate determined by cosmogenic surface dating on the Xidatan segment of the Kunlun fault (Qinghai China), *Geology*, *26*(8), 695–698.

Van der Woerd, J., F. J. Ryerson, P. Tapponnier, A. S. Meriaux, Y. Gaudemer, B. Meyer, R. C. Finkel, M. W. Caffee, G. G. Zhao, and Z. Q. Xu (2000), Uniform Slip-Rate along the Kunlun Fault: Implications for seismic behaviour and large-scale tectonics, *Geophys. Res. Lett.*, *27*(16), 2353–2356.

Van der Woerd, J., X. Xu, H. B. Li, P. Tapponnier, B. Meyer, F. J. Ryerson, A. S. Meriaux, and Z. Q. Xu (2001), Rapid active thrusting along the northwestern range front of the Tanghe Nan Shan (western Gansu China), *J. Geophys. Res.*, *106*(B12), 30,475–30,504.

Van der Woerd, J., A.-S. Meriaux, Y. Klinger, F. J. Ryerson, Y. Gaudemer, and P. Tapponnier (2002a), The November 14th, 2001 *Mw* = 7.8 Kokoshili earthquake in northern Tibet (Qinghai Province China), *Seismol. Res. Lett.*, *73*, 125–135.

Van der Woerd, J., P. Tapponnier, F. J. Ryerson, A. S. Meriaux, B. Meyer, Y. Gaudemer, R. C. Finkel, M. W. Caffee, G. G. Zhao, and Z. Q. Xu (2002b), Uniform postglacial slip-rate along the central 600 km of the Kunlun Fault (Tibet), from Al-26, Be-10, and C-14 dating of riser offsets, and climatic origin of the regional morphology, *Geophys. J. Int.*, *148*, 356–388.

Wang, E., J. L. Wan, and J. Q. Liu (2003), Late Cenozoic geological evolution of the foreland basin bordering the West Kunlun range in the Pulu area: Constraints on timing of uplift of northern margin of the Tibetan Plateau, *J. Geophys. Res.*, *108*(B8), 2401, doi:10.1029/2002JB001877.

Washburn, Z., J. R. Arrowsmith, S. L. Forman, E. Cowgill, X. F. Wang, Y. Q. Zhang, and Z. L. Chen (2001), Late Holocene earthquake history of the central Altyn Tagh fault, China, *Geology*, *29*(11), 1051–1054.

Winograd, I. J., J. M. Landwehr, K. R. Ludwig, T. B. Coplen, and A. C. Riggs (1997), Duration and structure of the past four interglaciations, *Quat. Res.*, *48*, 141–154.

Wittlinger, G., P. Tapponnier, G. Poupinet, J. Mei, S. Danian, G. Herquel, and F. Masson (1998), Tomographic evidence for localized lithospheric shear along the Altyn Tagh fault, *Science*, *282*, 74–76.

Yang, J., Z. Xu, J. Zhang, C.-Y. Chu, R. Zhang, and J. G. Liou (2001), Tectonic significance of early Paleozoic high-pressure frock in the Altun-Qaidam-Qilian Mountains, northwest China, in *Paleozoic and Mesozoic Tectonic Evolution of Central Asia:From Continental Assembly to Intra-continental Deformation*, edited by M. S. Hendrix and G. A. Davis, *Mem. Geol. Soc. Am.*, *194*, 151–170.

Yin, A., T. M. Harrison, F. J. Ryerson, W. J. Chen, W. S. F. Kidd, and P. Copeland (1994), Tertiary structural evolution of the Gangdese thrust system, southeastern Tibet, *J. Geophys. Res.*, *99*(B9), 18,175–18,201.

Yin, A., et al. (2002), Tectonic history of the Altyn Tagh fault system in northern Tibet inferred from Cenozoic sedimentation, *Geol. Soc. Am. Bull.*, *114*, 1257–1295.

Yue, Y. J., B. D. Ritts, and S. A. Graham (2001), Initiation and long-term slip history of the Altyn Tagh fault, *Int. Geol. Rev.*, *43*(12), 1087–1093.

Yue, Y., B. D. Ritts, S. A. Graham, J. L. Wooden, G. G. Gehrels, and Z. T. Zhang (2004), Slowing extrusion tectonics: Lowered estimate of post-early Miocene slip rate for the Altyn Tagh fault, *Earth Planet. Sci. Lett.*, *217*, 111–122.

M. W. Caffee, Physics Department, Purdue University, 1396 Physics Building, West Lafayette, IN 47907-1396, USA. (mcaffee@physics.purdue.edu)

R. C. Finkel, A.-S. Mériaux, and F. J. Ryerson, Lawrence Livermore National Laboratory, Earth Sciences Div/L-219, P.O. Box 808 L-206, Livermore, CA 94550, USA. (finkel1@llnl.gov; meriaux1@llnl.gov; ryerson@llnl.gov)

P. Tapponnier, Laboratoire de Tectonique, Mécanique de la Lithosphère, UMR 7578 Centre National de la Recherche Scientifique, Institut de Physique du Globe de Paris, 4 place Jussieu, F-75252 Paris Cedex 05, France. (tappon@ipgp.jussieu.fr)

J. Van der Woerd, IPGS-EOST, 5, rue Rene Descartes, F-67084 Strasbourg Cedex, France.

X. Xu, Seismological Bureau, 63 Fuxing Ave., Beijing 100036, China. (xxiwei@public3.bta.net.cn)

Z. Xu, Institute of Geology, Ministry of Land and Resources, Baiwanzhuand Rd., Beijing 100037, China. (xuzhiqin@ccsd.org.cn)